

Experimental Transport of Intensity Diffraction Tomography

by

Justin Wu Lee

B.S., Massachusetts Institute of Technology (2008)

Submitted to the Department of Mechanical Engineering
in partial fulfillment of the requirements for the degree of

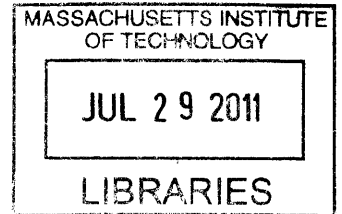
Master of Science in Mechanical Engineering

at the

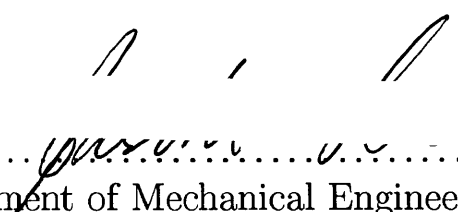
MASSACHUSETTS INSTITUTE OF TECHNOLOGY

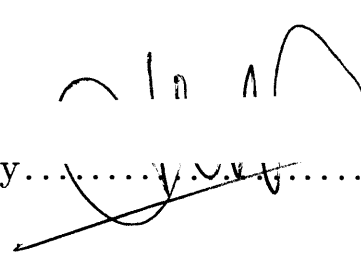
June 2011

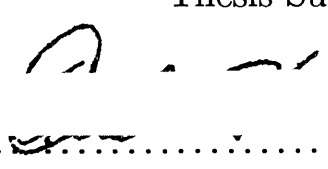
© Massachusetts Institute of Technology 2011. All rights reserved.



ARCHIVES

Author 
Department of Mechanical Engineering
May 18, 2011

Certified by 
George Barbastathis
Professor
Thesis Supervisor

Accepted by 
David E. Hardt
Chairman, Department Committee on Graduate Theses

Experimental Transport of Intensity Diffraction Tomography

by

Justin Wu Lee

Submitted to the Department of Mechanical Engineering
on May 18, 2011, in partial fulfillment of the
requirements for the degree of
Master of Science in Mechanical Engineering

Abstract

In this thesis, I perform intensity-based tomographic phase imaging in two ways. First, I utilize the paraxial transport of intensity equation (TIE) to construct phase maps of a phase object at multiple projection angles and reconstruct the object 3-dimensionally using basic tomographic principles. Then, I use an Intensity Diffraction Tomography (IDT) approach to improve the quality of reconstruction by accounting for diffraction effects under 1st order Rytov Approximation. I improve both approaches by applying compressive sensing techniques to estimate missing points in the undersampled data. Finally, I compare I-DT with single-shot, Gabor-type digital holography (also integrating use of compressive sensing principles) and discuss improvements and extensions of the presented implementation of IDT.

Thesis Supervisor: George Barbastathis
Title: Professor

Acknowledgments

I dedicate this work to my mother and brothers who have been unbearably patient with me during my continuing tenure at MIT.

I am extremely appreciative for my advisor, whose belief in “serendipitous discovery” has let my creativity flourish and for my wonderful group members, whose companionship and inputs have shaped the past two years of my life.

I am thankful for the enormous help I have received from Laura Waller and Se Baek Oh in helping me understand phase imaging/Transport of Intensity Imaging. I am thankful for Lei Tian, who has been my go-to person (along with Se Baek) whenever I have any optics questions/ponderings in mind. I am grateful to have worked with and befriended Yuan Luo, who has been like an older brother to me. I am also grateful to the members in 3-473m: Jason Ku, Nader Shaar, Johnny Choi, and Chi Chang for our fruitful discussions on issues ranging from research roadblocks to startup ideas. I would also like to thank everyone else in the 3D Optical Systems group for making my time as a Master’s student thoroughly enjoyable.

Contents

1	Introduction	17
1.1	Motivation	18
1.2	Tomography	19
1.3	Phase Imaging	20
1.4	Compressive Sensing	21
1.5	Scope of this work	21
2	Tomography	23
2.1	Principles of Tomography	23
2.1.1	Projections and the Radon Transform	24
2.1.2	Reconstruction Considerations & the Inverse Radon Transform	26
2.1.3	Applications	29
2.2	Diffraction Tomography	30
2.2.1	Basic Principles	30
2.2.2	Born Approximation	34
2.2.3	Rytov Approximation	35
2.2.4	Fourier Diffraction Projection Theorem	38
2.2.5	Reconstruction Issues	39
2.2.6	Applications	41
3	Phase Imaging & the Transport of Intensity Equation	43
3.1	Interferometric Phase Retrieval	43
3.2	Iterative Phase Retrieval	45

3.3	Digital Holography	47
3.4	Transport of Intensity	48
4	Compressive Sensing	51
4.1	Theory	52
4.2	Applications	54
4.2.1	Incomplete Fourier Measurements	54
4.2.2	Compressive Tomography	57
4.2.3	Image Restoration	58
4.3	Compressive Digital Holography	60
4.3.1	Theory	60
4.3.2	Experiment	62
5	Intensity-Based Phase Tomography	69
5.1	Background/Motivation	69
5.2	Experiment: Diffractionless Assumption	72
5.3	Measuring the Index of the Diamond	77
5.4	Intensity Diffraction Tomography	77
5.5	Measuring Diamond Dimensions	81
5.6	Comparison of Reconstructions	81
5.7	Compressive Intensity Tomography	82
5.8	Conclusions and Extensions: Toward Real-Time Phase Tomography .	85
5.8.1	Dual-camera TIE	85
5.8.2	SLM-based defocus system	85
5.8.3	Volume Holographic TIE Tomography	86
5.8.4	Color TIE Tomography	86
5.8.5	Application Real-time phase imaging flow cytometer	86
A	Derivations	87
A.1	TIE Derivation	87
A.2	TIE-IDT equivalence [12]	88

A.3 Fourier Diffraction Theorem	90
---	----

List of Figures

1-1	Cells are good examples of phase objects. They delay the light passing through it but do not alter the amplitude in any appreciable amount. Thus, there is little information in the amplitude/intensity at the detector plane, but much information in the phase of the field at the detector plane.	19
2-1	Steps of tomographic reconstruction	24
2-2	A projection through an “MIT” object	25
2-3	Radon Transform of object in Figure 2.2	25
2-4	Fourier Slice Theorem	27
2-5	Gridding is necessary for Fourier-Domain reconstruction since the polar coordinates do not align with the cartesian coordinates	28
2-6	Fourier Domain coverage by tomography. Low frequencies are over-sampled relative to higher frequencies.	28
2-7	Medical CT. Medical CT scanners return images of cross-sections of patients. The figure on the right is an image of patient abdomen. . .	29
2-8	k_x and k_y components of the waves are constrained to lie within the k-sphere. The magnitude of the combined vector components is $k_0 = \frac{2\pi}{\lambda}$. 31	31
2-9	Fourier Diffraction Projection Theorem [6]	39
2-10	Grid-driven vs. Data-driven interpolation [14]	40
3-1	Overview of Different Methods for Phase-Retrieval	44
3-2	A Michelson Interferometer used to retrieve phase information from a pure-phase object.	44

3-3	Fourier Space coverage of synthetic aperture tomography.	46
3-4	Iterative phase retrieval “ping-pongs” back and forth, applying constraints at the object and image planes, until a final answer is converged upon.. . . .	47
3-5	Transport of Intensity as conservation of mass	49
3-6	Transport of Intensity Simulation	50
3-7	(Left) Original phase at input plane. (Right) Phase retrieved via application of TIE. Magnitudes of retrieved phase do not take into account scale factor in the data.	50
4-1	Compressive Sensing Reconstruction based on knowledge that an object is sparse in its L0-norm (majority of its coefficients are 0 in domain of interest) “grows” along the axes instead of minimizing the L2-norm (“growing a circle”). In practice, solving minimizing the L0-norm is NP-hard, so the L1-norm is minimized instead (“growing a diamond”).	53
4-2	Compressive reconstruction of sparse signal from limited number of random Fourier-Domain measurements.	55
4-3	Compressive reconstruction of sparse signal from low-frequency Fourier-Domain measurements	56
4-4	Even when the object itself is not sparse, compressive sensing methods may still work by minimizing some other norm such as the Total Variation Norm (L1 of the gradient of the image). An overwhelming majority of objects man-made/nature-made are “smooth” (sparse in wavelet domain and TV norm) and will not correlate with noise. . . .	57
4-5	Compressive Sensing can be used for exact tomographic reconstruction from a limited number of angles of projection	58

4-6	Compressive Sensing can be used to reconstruct an image based on a tiny subset of pixels. The reconstruction adds the <i>a priori</i> information that the image is smooth. Reconstruction quality can be improved if the image is known/assumed to be sparse in a particular tailored dictionary domain.	59
4-7	In-line digital holography setup	63
4-8	Digital Hologram of bubbles images with the setup in the preceding figure	64
4-9	Simulated Hologram with 10 particles at different z depths	66
4-10	Compressive Reconstruction of several planes of the volume from simulated hologram. Bubbles show localization to the correct plane. . . .	67
4-11	Volume-rendered Compressive Reconstruction of entire volume of recorded hologram from Figure 4-8	67
5-1	A glass diamond index-matched to its surrounding media was used for this experiment. Placing the diamond in the oil turns it “invisible” to our eyes (it delays light passing through it but does not alter its amplitude/intensity)	71
5-2	A smaller version of the diamond in the preceding figure was used for this experiment. The diamond was mounted on an inverted rotation stage so that images could be acquired in a tomographic fashion. . .	71
5-3	Experimental Setup	72
5-4	Images were captured in-focus, over-focused, and under-focused. Background-subtraction was applied via pixel-wise division before processing. . . .	73
5-5	Applying the Transport of Intensity Equation to the defocused images results in a phase map representing the approximate phase depth/thickness of the object.	74
5-6	Volume-Rendered reconstruction of the object. Features such as edges are discernible.	75

5-7 Reconstructed Diamond after segmentation via thresholding and connectivity constraints. 76

5-8 Attempts to reconstruct the object from the original images alone result in a “shell” - the edges of a diamond are slightly discernible due to scattering effects, but otherwise the diamond is not detectable . . . 76

5-9 Setup: Measurement of Fresnel Reflection Coefficients 78

5-10 Fresnel coefficient curve-Fitting for s-polarized light. x-axis is angle of incidence/reflection, y-axis is normalized intensity ratio 78

5-11 Fresnel coefficient curve-fitting for p-polarized light. x-axis is angle of incidence/reflection, y-axis is normalized intensity 80

5-12 Diamond Schematic. The shape of the diamond was approximated from the object outline in the in-focus image, and object dimensions were measured with a caliper. 82

5-13 The TIE-based reconstruction does not match the dimensions of the diamond very well. 82

5-14 The IDT-based reconstruction more accurately matches the dimensions of the diamond. 83

5-15 Volumetric reconstruction of object: (left) without TIE or IDT (middle) with TIE (right) with IDT. The TIE reconstruction has more well-defined edges, but the volume/dimensions of the object reconstructed is not as accurate as that in the IDT reconstruction 83

5-16 Compressive Diffraction Tomography reconstruction from limited view-angles. (left) original image. (middle) Fourier-space coverage from synthetic aperture diffraction tomography, (right) recovered image . . 84

5-17 Convergence of the Compressive Sensing Solver, TwIST 84

List of Tables

5.1	Data collected for index measurement based on Fresnel Coefficient. Incident light had an intensity value of 0.91 ± 0.01	79
-----	--	----

Chapter 1

Introduction

A phase object is any object that delays the path of light wave without changing its amplitude. This tiny delay in the path length of light passing through the object is indiscernible to the human eye (as well as standard camera detectors), which can only sense light intensities. As a result, phase objects appear “invisible” to us. Mathematically, such objects are described as having an index of refraction that is entirely real.

If the difference in index of refraction between a phase object and its surrounding media is small, then the object is a “weak phase object,” and standard detectors (including the human eye) cannot detect the presence of the object at all. (e.g., one can clearly see the edges of a clear piece of glass in air, but if that piece of glass is immersed in mineral oil, then the edges of the glass are no longer observable and the object is no longer discernable, See Figure 5-1)

Weak phase objects are abundant in nature, and examples include jellyfish, lenses in the eyes of animals, and cellular organelles (immersed in water/cytoplasm). Since many biologically relevant creatures/objects are phase objects, it would be helpful to have an imaging system capable of making such objects visible in a quantitative fashion to detectors.

The contents of this work focus on implementing an imaging system capable 3-dimensional reconstruction of phase objects from intensity/amplitude measurements alone. Bringing together concepts from the fields of tomography, phase imaging,

and compressive sensing, this work experimentally demonstrates an imaging system capable of retrieving the 3-dimensional complex index distribution of phase objects. Permutations of these topics will be discussed, and experimental results will be shown. Such a system has the ability to offer greater detail in imaging phase objects and would significantly benefit the medical imaging community (e.g. live cell imaging in pathology). Potential extensions of this work, including a real-time imaging system for flow cytometry is discussed in the concluding section of this work.

1.1 Motivation

Any one who's ever looked through a clear window has seen a phase object (the window). Phase objects do not alter the intensity of the light passing through it, and when looking through a clear window, one cannot tell if the window was there or not to begin with (or how thick the window is). In this sense, the window is "invisible" to our eyes.

The keen reader will note that we can actually see the presence of a clear pane of glass (although not its thickness) at its edges, and indeed, if we look at the edges of a clear pane of glass, we see the strongly scattered light at the edge of the glass/air interface. In general, if the difference in index of refraction between a phase object and its surround media (or within itself) is great enough, then we will notice the scattering of light as it scatters within/at the edges of the object.

If the difference between the index of refraction of an object and its surrounding media is small, then the object is termed a "weak phase object," and the edges of the object are no longer visible to the human eye. The presence of an object can still be determined by defocusing the image of the object upon a detector [1, 2], but quantifying the index difference between the object and its surrounding media cannot be done from a single image.

Examples of weak phase objects include: jellyfish in water, cellular organelles (cell organelles have indices of refraction that are very close to that of their surrounding media), and packets of heated air (e.g., just above a candle flame). In the case of the

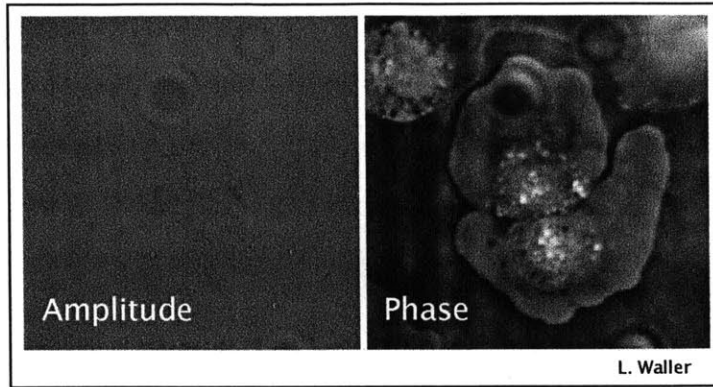


Figure 1-1: Cells are good examples of phase objects. They delay the light passing through it but do not alter the amplitude in any appreciable amount. Thus, there is little information in the amplitude/intensity at the detector plane, but much information in the phase of the field at the detector plane.

third example, if the temperature differences are high enough (or change fast enough), then the presence of the heating is visible as a disturbance of light from behind the heated air packet [3].

The frequency of illuminating light plays a role in determining whether or not an object is a “phase object” and determines the scattering effects that will need to be considered when imaging the object. For instance, a piece of glass index-matched to surrounding mineral oil may be a phase object at optical frequencies (primarily Rayleigh/Mie scattering), but it is not a phase object at X-ray frequencies (Compton Scattering). At X-ray frequencies, objects scatter so strongly that a different model is used (instead of weakly scattering models used in optical-regime phase imaging). “[4 Attenuation” of (straight) rays of X-rays makes the glass an “amplitude object.”

This work will focus predominately on optical-regime phase objects. In general, this regime is the most biologically relevant for applications such as clinical pathology.

1.2 Tomography

Computed Tomography is the process of reconstructing a 2-Dimensional slice of an object from projections of some parameter that object. Recently, the technique has gained wide popularity in the fields of medical imaging for devices such as CT and

PET scanners. While CT and PET scanners collect data from photons in the X-ray regime, this work focuses on tomography of phase objects in the visible light regime.

In the visible regime, tomography is a much more difficult task since scattering effects cannot be lumped together as “attenuation.” Additionally, modern detectors can only detect the intensity of light, not the phase of the wave. The experiments presented in this work overcome these two issues by combining techniques of diffraction tomography (for scattering effects) and transport of intensity imaging (to retrieve phase from intensity information alone).

Diffraction Tomography is a method to account for weak scattering effects in an imaged object. While tomographic inversion of collected data (to retrieve the object function) typically employs use of the Fourier Slice Theorem, a related theorem, the Fourier Diffraction Projection Theorem (which fills in arcs in Fourier Space instead of lines) is used when diffracting effects cannot (or should not) be ignored [5, 6]. Effects of weak diffraction in the optical regime are typically modeled under first order Born or Rytov approximations.

1.3 Phase Imaging

Various methods exist to image phase objects. Some are qualitative (e.g., phase-contrast microscopy), and other are quantitative (e.g., phase-unwrapped interferometric microscopy and transport of intensity imaging). Quantification of the phase of an uniform-index object is equivalent to determining how thick that object is. In general, quantification of phase gives the “optical thickness” of that object (in this sense, the measured phase is a projection of sorts), and tomographic reconstruction can determine the 3-D index of refraction profile of a phase object of interest.

Although intensity-based phase retrieval can be performed for a wide range of illuminating frequencies, (including X-rays under special circumstances [7]), this work focuses on the use of the Transport of Intensity Equation (TIE) for imaging of phase objects. The TIE measures the intensity imaged at multiple planes in order to reconstruct the full field (amplitude and phase) at a plane between the measured planes

[8, 9]. The transport of intensity equation is a conservation of flux equation and will be discussed more in Chapter 3.

1.4 Compressive Sensing

Compressive sensing is a recently-developed framework for the systematic use of sparsity priors to improve estimates of solutions to under-determined linear systems. [31] Elements of compressive sensing theory can be applied to reduce noise in tomographic reconstructions as well as to reduce the number of measurements required for accurate reconstruction. In this work, compressive sensing is applied to various imaging geometries (e.g., plane wave/regular, synthetic aperture, etc.) both in simulations and experimentally to improve the quality of reconstructions.

1.5 Scope of this work

Chapters two through four give an overview to the fields and theories of tomography, phase imaging, and compressive sensing. Although each chapter can be read independent of the others, emphasis is placed on the combination of techniques.

Chapter five presents the experimental setup and results for TIE tomography and Intensity Diffraction Tomography (IDT). Data collection and Processing steps are outlined, and graphical results are shown. Potential variations to tomographic phase imaging are discussed, with the objective of moving towards a real-time 3D phase imager. Examples include: (1) volume holographic IDT, (2) Dual-camera IDT, (3) real-time IDT from chromatic aberration, (4) SLM-defocus IDT, and (5) Structured Illumination IDT. Since registration is an issue for many of these methods, the chapter will include a brief discussion of various image registration methods (cross-correlation, maximization of mutual information, minimizing joint entropy, minimizing least-square error, etc.)

Chapter five concludes with a recapitulation of concepts in the work and discussion of potential future work and applications (real-time flow cytometer) of intensity-based

phase tomography.

Chapter 2

Tomography

Computed Tomography is a mathematical algorithm for tomographic reconstruction from projection data (reconstruction of a slice of information based on captured projections of that information). The projections can be attenuation of x-rays through an object (as in the case of traditional x-ray CT scanners) or “total phase delay” of a weak phase object (as in the case of phase tomography of weak objects without accounting for diffraction). This chapter will discuss the basic concepts of computed tomography. It will also discuss diffraction tomography and the various assumptions and processes involved in reconstruction from incomplete Fourier-Space measurements.

2.1 Principles of Tomography

Tomographic reconstruction is a two-step process. First, projections of some feature of an object are captured at multiple view-angles. Then, the information in these projections is processed to reconstruct slices of the feature-of-interest (the one captured from the projections) of the original object.

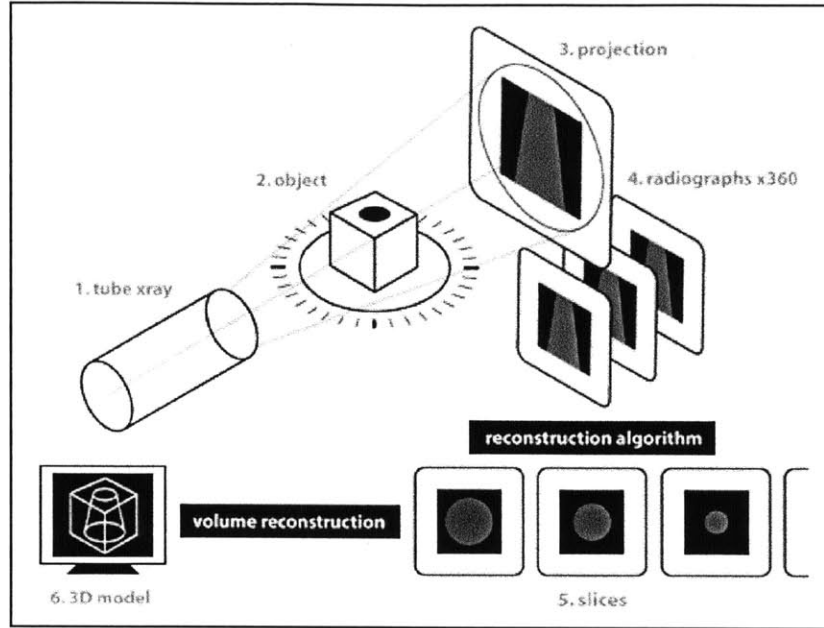


Figure 2-1: Steps of tomographic reconstruction

2.1.1 Projections and the Radon Transform

A projection of some property of an object is given by the equation:

$$P(\theta) = \int_{l(\theta, x')} p(x, y) ds \quad (2.1)$$

where the line integral above denotes the straight line integral of the parameter p through the object. The location and orientation of the line is demarcated by θ and x' . The projection of an object is the sum/integral of that object along the red rays “projected” onto a new axis tilted at a specific angle. Figure 2-2 illustrates a projection through an “MIT” object at an angle of $\theta = 10^\circ$. Using trigonometric properties and the delta function, the mathematical description of a projection can be rewritten as:

$$P(\theta, x') = \int_{-\infty}^{\infty} \int_{-\infty}^{\infty} p(x, y) \delta(x \cos \theta + y \sin \theta - x') dx dy \quad (2.2)$$

A 360° collection of projections about an object through is known as the Radon

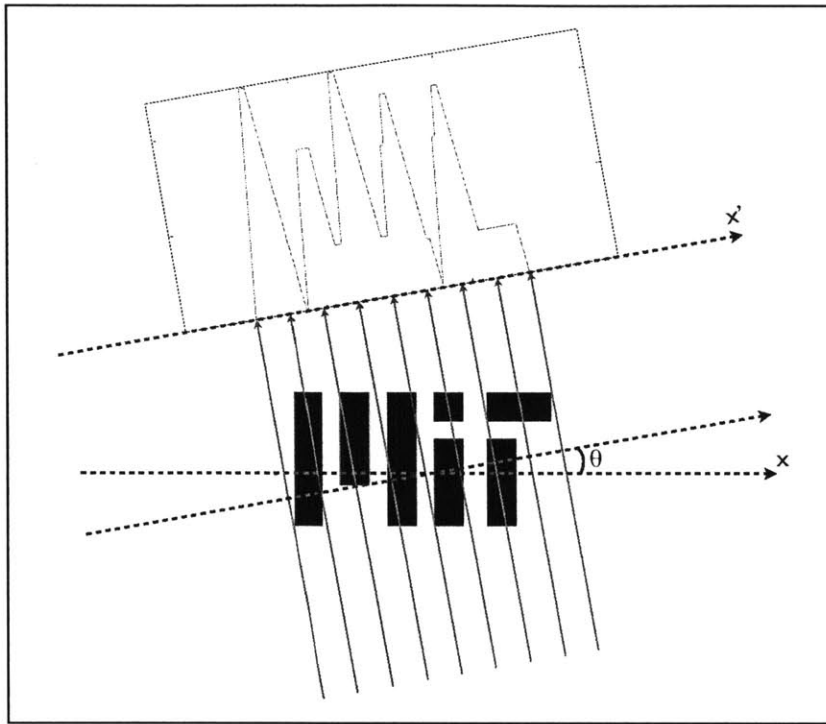


Figure 2-2: A projection through an "MIT" object

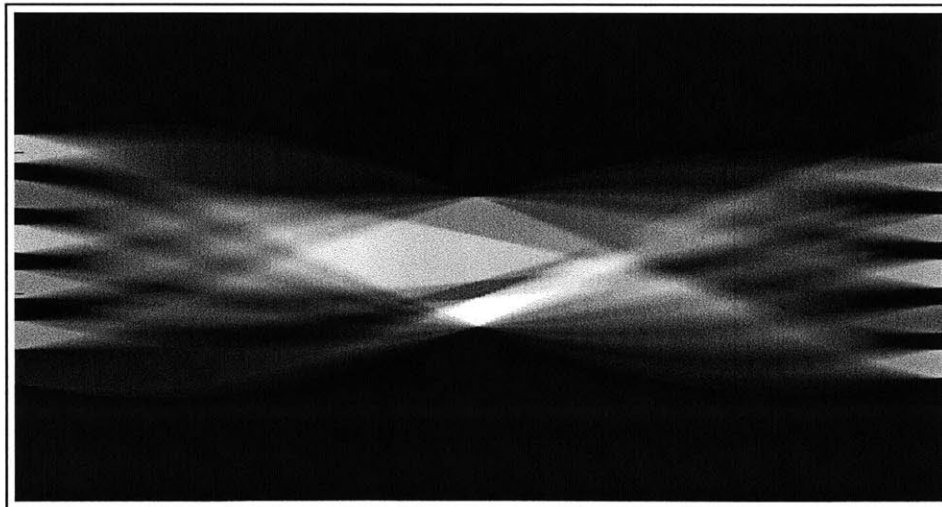


Figure 2-3: Radon Transform of object in Figure 2.2

Transform of the object (Figure 2-3). Based on the features of the Radon transform, information/descriptions of the object can be determined. Theoretically, all of the information of the (non-scattering) object is present within the radon transform, but the transform itself does not lend itself to easy understanding of what the object looks like (although a trained eye could pick out corners and edges of an object from a sinogram fairly easily). Thus, in order to recover the object itself (in a representation that is intuitive to understand), further computation must be performed.

2.1.2 Reconstruction Considerations & the Inverse Radon Transform

Central to tomography is the Fourier Slice Theorem, which states that:

$$F(u, 0) = S_{\theta=0}(u) \quad (2.3)$$

In the above equation, $F(u, 0)$ denotes the value of the 2D Fourier Transform of the object along the $v = 0$ line in the frequency domain, and $S_{\theta=0}(u)$ represents the 1-dimensional Fourier Transform of the projection at $\theta = 0$.

$$S(\theta, u) = \int_{-\infty}^{\infty} P(\theta, x') e^{j2\pi ux'} dx' \quad (2.4)$$

In other words, the 1D Fourier Transform of the projection is equivalent to a line in the 2D Fourier Transform of the object (Figure 2-4, Proof in Appendix). The results obtained above are independent of the orientation between the object and the coordinate system. Thus, if a projection is acquired at an angle θ relative to the original measurement, then the 1D Fourier Transform of that projection is equal to a line in the 2D Fourier Transform of the object which has an angle of θ to the u-axis.

Formulation of the tomographic reconstruction process in Fourier Space presents two problems. First, the Fourier Slice Theorem is a continuous theorem and does not account for the discrete values of the sampled data (as one would need when doing

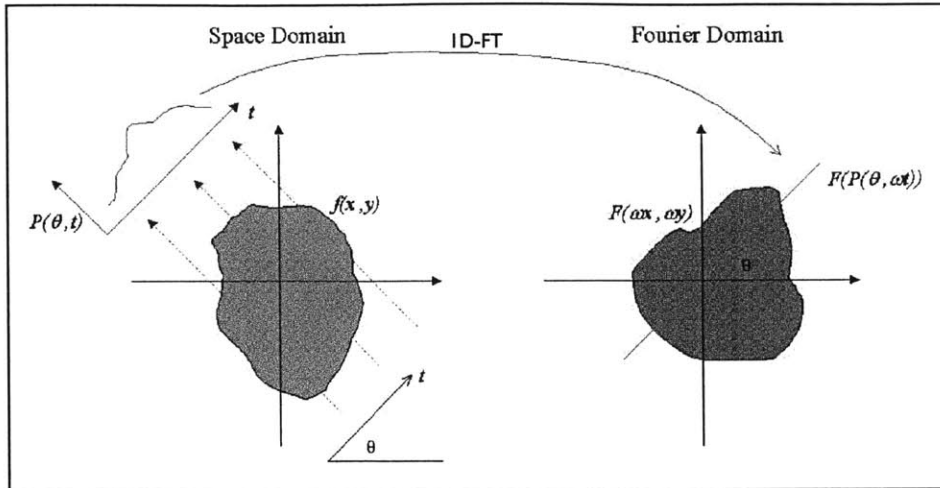


Figure 2-4: Fourier Slice Theorem

numerical computation). The problem is illustrated in the figure below; when doing numerical computation, the 2D Fourier Transform values at discrete coordinates are required for reconstruction, but even with infinite spatial resolution of projections (very finely sampled), unless an infinite number of angles are measured as well, one cannot exactly determine the appropriate value of the pixel. that corresponds with the measured point (which is in polar coordinates).

A second problem with the Fourier Space formulation of tomographic reconstruction is that minor errors in the frequency domain can lead to significant global errors in the reconstructed data. This presents problems for processes which fill in empty regions of Fourier Space using traditional interpolation methods.[4, 6]

The Inverse Radon Transform sidesteps these problems by simply “back-projecting” each projection through the object and summing the projections to retrieve an estimate of the object. Since the center of the object is ”oversampled” relative to other points in the object (Figure 2-6), appropriate weighting functions need to be applied to the data. The necessity of weighting higher frequencies more heavily than lower frequencies when back-projecting is illustrated in Figure 2-6. Typically, a triangular, Hamming, or Hann window is used to compensate for the “overweighting” of central frequencies.

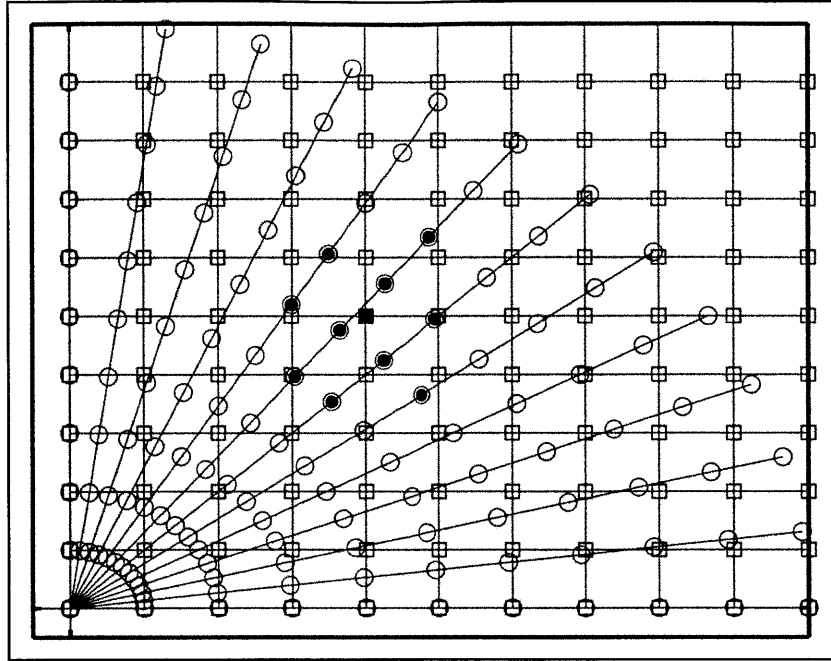


Figure 2-5: Gridding is necessary for Fourier-Domain reconstruction since the polar coordinates do not align with the cartesian coordinates

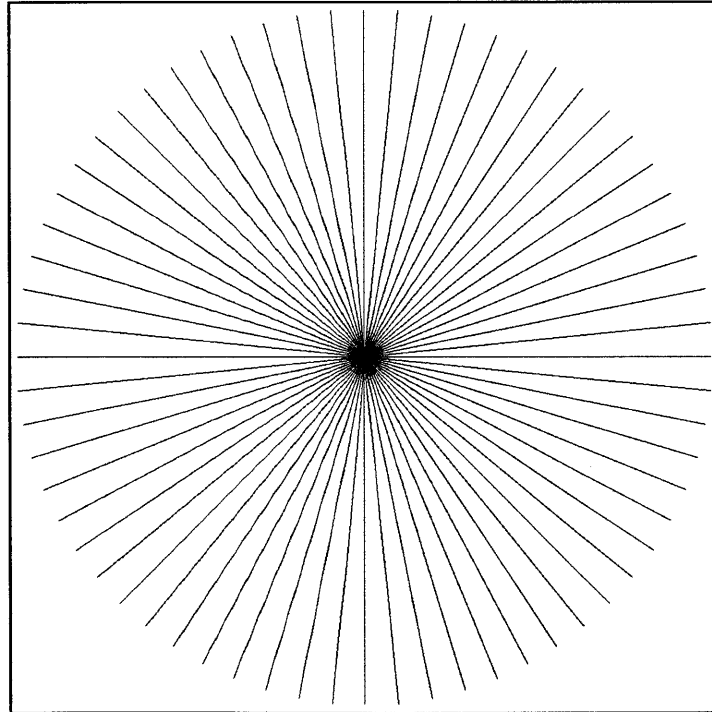


Figure 2-6: Fourier Domain coverage by tomography. Low frequencies are oversampled relative to higher frequencies.

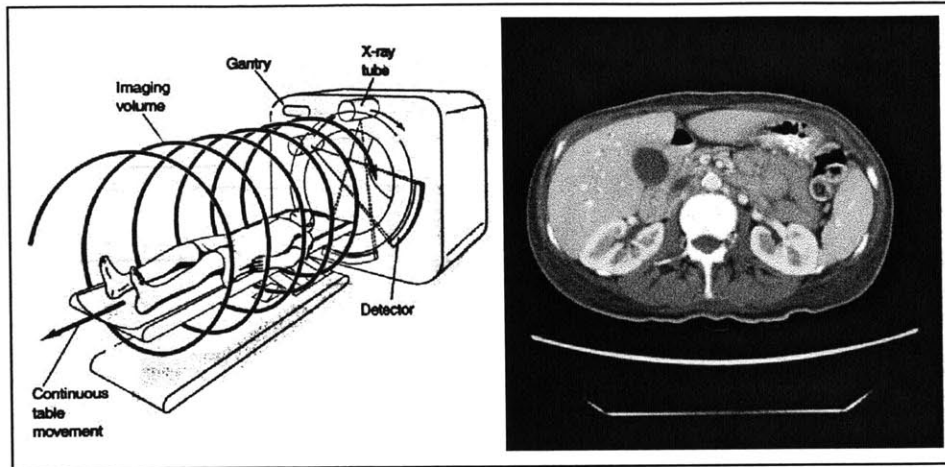


Figure 2-7: Medical CT. Medical CT scanners return images of cross-sections of patients. The figure on the right is an image of patient abdomen.

When the radon transform cannot be used (as in the case of diffraction tomography), the individual problems have to be addressed individually and conventional solutions to the above problems are discussed later in this chapter.

2.1.3 Applications

Computed Tomographic Reconstruction has been used widely in medical imaging, predominately for X-ray regime imaging processing such as CT scans (Fig. 2-7) or PET scans. In medical CT imaging, the real part of the attenuation coefficient is measured and the "attenuation coefficient" (percent of incident x-rays that reach the detector) of x-rays passing through human/animal tissue). If a pure phase object is imaged, lower-energy light can be used (e.g. - visible light) and the total phase delay of the measured (as in the case of TIE or interferometric methods) to determine the phase delay introduced by the object. Depending on the object, its surrounding media, and the frequency of the illuminating light, diffraction effects may need to be considered during tomographic reconstruction.

2.2 Diffraction Tomography

Diffraction Tomography is a method related to traditional tomography that accounts for diffracting effects of the object. Under simplifying assumptions, a weakly-scattering object can be reconstructed to greater accuracy than if diffraction were not accounted for. Instead of the 1D Fourier Transform of each projection filling in lines in the 2D Fourier Space of the object, the 1D Fourier Transforms of the “scattered projections” fill in *arcs* in the 2D Fourier Space of the Object.

Diffraction tomography (DT) is an image reconstruction technique used to retrieve the complex refractive index of a weakly scattering object from measured wavefronts. The technique has found its way into a wide variety of applications, and has proven particularly useful in the fields of cell biology and pathology to elucidate cellular and intracellular features without the use of fluorescent contrast agents or proteins. The organelles of a cell can be considered weakly scattering phase objects since they have indices of refraction close to that of cellular cytoplasm. In general, samples of biological interest tend to contain little or no amplitude information but have well-defined phase structure. The samples diffract/scatter light weakly, and thus, there has been a strong motivation to develop imaging techniques capable of three-dimensional phase-amplitude retrieval of weakly scattering phase objects.

2.2.1 Basic Principles

The fundamental theorem of diffraction tomography (Fourier Diffraction Theorem) posits that a measured field “projection” of an object (the forward-scattering field along a single plane of measurement) is equivalent to the Fourier Transform of an object over a semicircular arc in Fourier Space. Under cases of high frequency inputs, the Fourier Diffraction Theorem reduces to the Fourier Projection Theorem.

To better understand the reasoning behind the Fourier Diffraction Theorem, let us first begin with the homogeneous Helmholtz Equation.

$$[\nabla^2 + k^2(\vec{r})]\psi(\vec{r}, t) = 0 \tag{2.5}$$

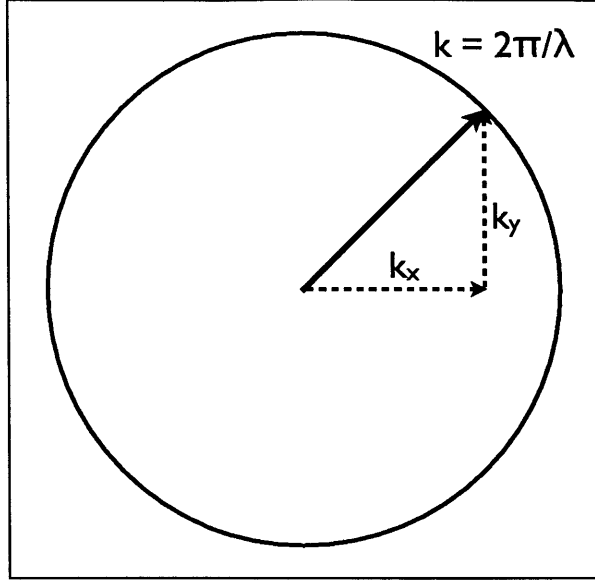


Figure 2-8: k_x and k_y components of the waves are constrained to lie within the k -sphere. The magnitude of the combined vector components is $k_0 = \frac{2\pi}{\lambda}$.

Suppressing the time dependence and noting that for homogeneous media (constant $n \rightarrow$ constant λ, k) yields:

$$[\nabla^2 + k_0^2(\vec{r})]\psi(\vec{r}) = 0 \quad (2.6)$$

Solutions to this equation are of the form $e^{j\vec{k}\cdot\vec{r}} = \psi(\vec{r})$ (plane wave), and one can think of all solutions as a weighted superposition of plane waves. If we consider the 2-D case for simplicity (and without loss of *generosity*, to borrow an expression from a labmate of mine), we have:

$$\psi(\vec{r}) = \frac{1}{2\pi} \int_{-\infty}^{\infty} \alpha(k_y) e^{j(k_x x + k_y y)} dk_y + \frac{1}{2\pi} \int_{-\infty}^{\infty} \beta(k_y) e^{j(-k_x x + k_y y)} dk_y \quad (2.7)$$

The above equation expresses a field that has been decomposed into 1-D plane wave components. For each k_y , there are only two possible k_x 's (+ or -) that satisfy $k_x^2 + k_y^2 = k_0^2$ (we have chosen to ignore evanescent waves, since their effects decay rapidly). Figure 2-8 illustrates this.

If we further constrain our setup to only right-ward propagating waves ($+\hat{x}$ direc-

tion), then the previous equation reduces to:

$$\psi(\vec{r}) = \frac{1}{2\pi} \int_{-\infty}^{\infty} \alpha(k_y) e^{j(k_x x + k_y y)} \quad (2.8)$$

Arbitrarily setting a measurement plane for the field (somewhere to the right of the sources) at $x = 0$, we have:

$$\psi(0, y) = \frac{1}{2\pi} \int_{-\infty}^{\infty} \alpha(k_y) e^{j(k_y y)} \quad (2.9)$$

From the equation above, we see that the field (“detected” at this plane is the 1-D Fourier transform of the weighting function, $\alpha(k_y)$, which denotes the coefficients of plane waves propagating to the right. In other words:

$$\alpha(k_y) = F\{\psi(0, y)\} \quad (2.10)$$

Once $\alpha(k_y)$ is determined, one can substitute the value back into equation 2.9 to determine the field anywhere to the Right-Hand-Side of the $x = 0$ plane. In summary, “If one knows the field at one plane (and that all sources are to the left of that plane), then he/she can get/determine the plane-wave breakdown of that field. Then, he can propagate each plane wave component to a distance, l , to the RHS of the measured plane/line.

Note: $\psi_{\text{plane wave}}(x = l, y) = \psi_{\text{plane wave}}(x = l_0, y) e^{jk_x(l_1 - l_0)}$

Returning to our homogeneous wave equation, we now make a slight modification to allow for weak index inhomogeneities.

$$[\nabla^2 + k(\vec{r})^2]\psi(\vec{r}) = 0 \quad (2.11)$$

Under scalar assumptions (ignoring polarization effects), $k(\vec{r})$ can be written as:

$$k(\vec{r}) = k_0 \cdot n(\vec{r}) = k_0 \cdot [n_0 + n_\delta(\vec{r})] \quad (2.12)$$

where n_0 is the index of refraction of the surrounding media and n_s denotes the perturbation/deviation of the index of refraction within a volume from the baseline index. Plugging this into the wave equation yields the following steps:

$$[\nabla^2 + k_0^2 n(\vec{r})^2] \psi(\vec{r}) = 0 \quad (2.13)$$

$$\nabla^2 \psi(\vec{r}) = -k_0^2 n(\vec{r})^2 - k_0^2 + k_0^2 \psi(\vec{r}) \quad (2.14)$$

$$(\nabla^2 + k_0^2) \psi(\vec{r}) = -k_0^2 (n(\vec{r})^2 - 1) \psi(\vec{r}) \quad (2.15)$$

The first term on the Right-Hand-Side of 2.15 is known as the “scattering potential” of the object ($o(\vec{r}) = k_0^2 [n^2(\vec{r}) - 1]$) and after substitution the wave equation for small inhomogeneities can be written as:

$$(\nabla^2 + k_0^2) \psi(\vec{r}) = -o(\vec{r}) \psi(\vec{r}) \quad (2.16)$$

If the total field $\psi(\vec{r})$ is considered as the sum of the original incident field, $\psi_0(\vec{r})$ and the scattered field $\psi_s(\vec{r})$, then based on the knowledge that the original incident field (field present when there are no inhomogeneities) has the solution:

$$(\nabla^2 + k_0^2) \psi(\vec{r}) = 0 \quad (2.17)$$

We can substitute in this information and arrive at the following wave equation for just the scattered component of the field:

$$(\nabla^2 + k_0^2) \psi_s(\vec{r}) = -o(\vec{r}) \psi(\vec{r}) \quad (2.18)$$

This equation has a Green’s function solution, $g(\vec{r}|\vec{r}') = \frac{e^{jk_0 R}}{4\pi R}$ (zero-order Hankel function of the first kind; in the 3-D case, solution is just a spherical wave), which solves:

$$(\nabla^2 + k_0^2) g(\vec{r}|\vec{r}') = -\delta(\vec{r} - \vec{r}') \quad (2.19)$$

Representing the forcing function (RHS of equation 1.18) as a superposition of im-

pulses, we have:

$$o(\vec{r})\psi(\vec{r}) = \int o(\vec{r}')\psi(\vec{r}')\delta(\vec{r} - \vec{r}')d\vec{r}' \quad (2.20)$$

From the above summation description, the scattered field can now be re-written as a superposition (convolution):

$$\psi_s(\vec{r}) = \int g(\vec{r} - \vec{r}')o(\vec{r}')\psi(\vec{r}')d\vec{r}' \quad (2.21)$$

The integral above describes the scattered field, but the inputs (on the right hand side) are in terms of the total field ($\psi + \psi_s$). In order to solve the above equation for the scattered field, further simplifying assumptions are required. The two most common of these assumptions are the Born Approximation and the Rytov Approximation.

2.2.2 Born Approximation

Qualitatively, the Born Approximation can be described as "an incident wave upon the volume scatters just once from each point in that volume, and the strength of that scattering is determined by scattering potential." Earlier, it was shown that the total field can be considered the sum of the incident field and a (weaker) scattered field ($\psi(\vec{r}) = \psi_0(\vec{r}) + \psi_s(\vec{r})$). Plugging this into the last equation of the previous section yields:

$$\psi_s(\vec{r}) = \int g(\vec{r} - \vec{r}')o(\vec{r}')\psi_0(\vec{r}')d\vec{r}' + \int g(\vec{r} - \vec{r}')o(\vec{r}')\psi_s(\vec{r}')d\vec{r}' \quad (2.22)$$

Under a "scatter once" assumption, the scattered field can be considered very small compared to ψ_0 and the second term in the above equation can be dropped. This results in the "First Order Born Approximation"

$$\psi_s(\vec{r}) \approx \psi_{B1}(\vec{r}) \approx \int g(\vec{r} - \vec{r}')o(\vec{r}')\psi_0(\vec{r}')d\vec{r}' \quad (2.23)$$

Under a “scatter twice” assumption, the ψ_0 in the above equation can be replaced by $\psi_0 + \psi_{B0}$. This results in the “Second Order Born Approximation”

$$\psi_{B2}(\vec{r}) \approx \int g(\vec{r} - \vec{r}') o(\vec{r}) [\psi_0(\vec{r}') + \psi_{B0}(\vec{r}')] d\vec{r}' \quad (2.24)$$

Higher-order Born Approximations can be written similarly as:

$$\psi(\vec{r}) \approx \psi_0(\vec{r}) + \psi_{B1}(\vec{r}) + \psi_{B2}(\vec{r}) + \dots \quad (2.25)$$

where each higher-order scattered field is the output due to an input field which is itself the Born field of one order less. The intuition behind this statement is premised upon iterative application of Huygen’s principle. Each point within the scattering object emits as a point source (weighted by the scattering potential of the object). The newly created field, which is weaker than the original incident field now causes the points within the object to emit as point sources yet again (weighted by both the incident field value and the scattering potential), and the process is repeated in the “Born Series” until a total field is converged upon.

The First-Order Born Approximation remains valid when the scattered field is much smaller than the incident field. For a thick homogeneous cylinder of radius a , the approximation holds if $an_\delta < \frac{\lambda}{4}$, where n_δ is the change in refractive index with respect to the surrounding media and λ is the wavelength of light used to illuminate. From the equation, we see that validity of the Born approximation depends on the *total* phase delay through the object. (change in the phase between the incident field and the wave propagating through the object must be less than π) [6].

2.2.3 Rytov Approximation

The Rytov approximation considers the total field as a complex phase, $\psi(\vec{r}) = e^{\phi(\vec{r})} = e^{(\phi_0(\vec{r}) + \phi_s(\vec{r}))}$, $\psi_0(\vec{r}) = e^{\phi_0(\vec{r})}$. Plugging this into our wave equation ($\nabla^2 \psi(\vec{r}) + k^2 \psi(\vec{r}) = 0$) yields:

$$\nabla^2 \psi(\vec{r}) + k^2 e^{\phi(\vec{r})} = 0 \quad (2.26)$$

$$\nabla [(\nabla\phi)(\psi(\vec{r}))] + k^2 e^\phi = 0 \quad (2.27)$$

$$\nabla^2\phi[\psi(\vec{r})] + (\nabla\phi)^2\psi(\vec{r}) + k^2\psi(\vec{r}) = 0 \quad (2.28)$$

Thus,

$$(\nabla\phi)^2 + \nabla^2\phi + k_0^2 = 0 \quad (2.29)$$

for homogeneous media, and

$$(\nabla\phi)^2 + \nabla^2\phi + k_0^2 = -o(\vec{r}) \quad (2.30)$$

for media with slight index inhomogeneities. Substituting in the complex phase representation of the field ($\phi(\vec{r}) = \phi_0(\vec{r}) + \phi_s(\vec{r})$) and rearranging the above equation yields:

$$(\nabla\phi_0)^2 + 2\nabla\phi_0 \cdot \nabla\phi_s + (\nabla\phi_0)^2 + \nabla^2\phi_0 + \nabla^2\phi_s + k_0^2 = -o(\vec{r}) \quad (2.31)$$

where the \vec{r} dependency of ϕ in the above equation has been suppressed to simplify notation. Now, subtracting the homogeneous solution (2.29) gives:

$$(\nabla\phi_s)^2 + 2\nabla\phi_0 \cdot \nabla\phi_s + \nabla^2\phi_s = -o(\vec{r}) \quad (2.32)$$

Linearization of Eqtn. 2.32 requires a bit of a diversion. First, let us consider the following application of the product rule:

$$\nabla^2(\psi_0\phi_s) = \nabla(\nabla\psi_0 \cdot \phi_s + \psi_0\nabla\phi_s) \quad (2.33)$$

Distributing and applying the product rule again, we have:

$$\nabla^2(\psi_0\phi_s) = \nabla(\nabla\psi_0 \cdot \nabla\phi_s) + \nabla(\psi_0\nabla\phi_s) = \nabla^2\psi_0 \cdot \phi_s + 2\nabla\psi_0\nabla\phi_s + \psi_0\nabla^2\phi_s \quad (2.34)$$

Now, considering that the input is a plane wave ($\psi_0 = Ae^{j\vec{k}\cdot\vec{r}}$), we have the relationship:

$$\nabla^2\psi_0 = -k_0^2\psi_0 \quad (2.35)$$

Plugging this into 2.34, we have:

$$2\psi_0 \nabla \phi_0 \cdot \nabla \phi_s + \psi_0 \nabla^2 \phi_s = \nabla^2 (\psi_0 \phi_s) + k_0^2 \psi_0 \phi_s \quad (2.36)$$

And substituting this back into 2.32 yields:

$$(\nabla^2 + k_0^2) \psi_0 \phi_s = -\psi_0 [(\nabla \phi_s)^2 + o(\vec{r})] \quad (2.37)$$

The above differential equation has the solution:

$$\psi_0 \phi_s = \int_{V'} g(\vec{r} - \vec{r}') \psi_0 [(\nabla \phi_s)^2 + o(\vec{r})] d\vec{r}' \quad (2.38)$$

The First-Order Rytov Approximation asserts that:

$$(\nabla \phi_s)^2 + o(\vec{r}) \approx o(\vec{r}) \quad (2.39)$$

The first order Rytov Approximation is valid when $o(\vec{r}) \gg (\nabla \phi_s)^2$ (when the *rate of change* of the scattered phase is small). The condition on the rate of change of the index of refraction can be written as [6]:

$$n_\delta \gg \frac{(\nabla \phi_s)^2}{k_0^2} \quad (2.40)$$

Using the Rytov Approximation, equation 2.38 reduces to:

$$\psi_0 \phi_s = \int_{V'} g(\vec{r} - \vec{r}') \psi_0(\vec{r}') o(\vec{r}') d\vec{r}' \quad (2.41)$$

This equation has the same form as the first order Born approximation for the scattered field. The difference is that the quantity on the left no longer corresponds to the scattered field (as it did under the born approximation), but is instead equal to the incident field times the complex phase of the scattered field ($\psi_0(\vec{r}) \cdot \phi_s(\vec{r})$).

2.2.4 Fourier Diffraction Projection Theorem

The simplest Diffraction Tomography setup involves illumination of the scattered object with a monochromatic plane wave. Under assumptions of weak scattering, scalar approximations may be employed, and the wave may be written as $\psi_0 e^{j(kr - wt)}$, where w is the frequency of the monochromatic plane wave, and $k = w/c$ is the wave number. Separating time and spatial dependencies, the incident wave may be written as: $\psi_i(r, t) = \psi_i(r) e^{-jwt}$.

As discussed earlier, the scattering object is characterized by a scattering potential $o(\vec{r})$, related to the complex refraction index of the material, $n(r)$, by: $o(r) = k_0^2 [n^2(r) - 1]$. If the index of refraction is slowly varying, then the first order Rytov approximation can be employed. Under this approximation, the total field (incident plus scattered) at the detector plane can be expressed as:

$$\psi(r) \approx \psi_i(r) e^{\phi(r)} \quad (2.42)$$

Continuing under the first Rytov approximation, the complex phase function is given by:

$$\phi(r) = \frac{1}{\psi_i(r)} \int_V o(r') \frac{e^{jk|r-r'|}}{r-r'} \psi_i(r') d^3 r' \quad (2.43)$$

The Fourier Diffraction (FDP) Theorem posits that (proof in appendix) [6, 5, 48, 24]:

$$\tilde{\Psi}(u, v, z = d) = \frac{(2\pi)^2 j}{w} O(u\hat{s}_1 + v\hat{s}_2 + (w - k)\hat{s}_0) e^{-j(ux+vy)} \quad (2.44)$$

where

$$\tilde{\Psi}(u, v, z) = \frac{1}{(2\pi)^2} \int \int_{\mathbb{R}^2} \phi(x, y, z) e^{-j(ux+vy)} dx dy \quad (2.45)$$

denotes the 2D Fourier Transform of the scattered phase. It is clear from this equation that the FT of the measured fields (e.g., retrieved from TIE of interferometry after phase unwrapping), should correspond to shifted hemispherical shells in Fourier Space (depending on which approximation is used, a logarithm may need to be first taken before application of the FDP theorem).

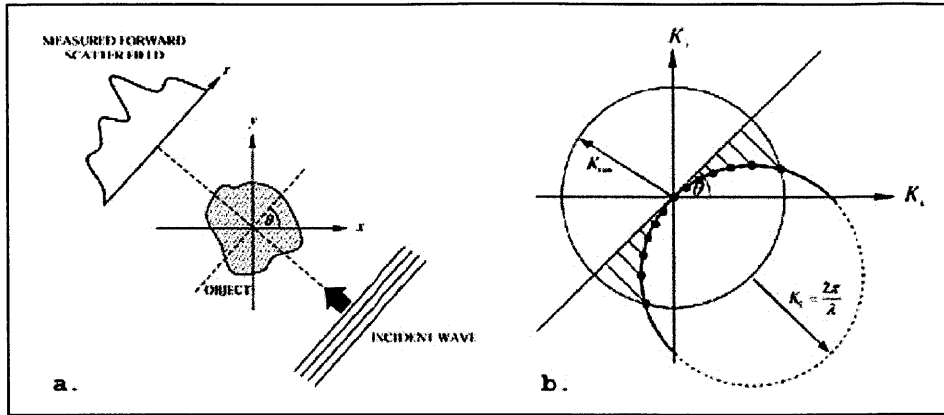


Figure 2-9: Fourier Diffraction Projection Theorem [6]

2.2.5 Reconstruction Issues

While computed tomography is typically performed using the inverse radon transformation (due to speed and simplicity of the algorithm - computations can be done as soon as projection data is acquired instead of having to wait for all the data to be acquired before doing all of the processing), diffraction tomography cannot. Instead, in order to reconstruct, one must use a back-propagation algorithm or else interpolate in Fourier Space.

Several methods have been proposed for efficient backpropagation algorithms. Slaney discusses a filtered backpropagation algorithm in [6] but concludes that interpolation in frequency space is a preferable option to this method. Another method for diffraction tomography reconstruction, proposed in [13], re-projects the “arcs” in Fourier Space to lines for use in a inverse radon transform algorithm.

For a more generalized reconstruction (including one that allows for different sampling patterns in Fourier Space, as one might see in MRI or a highly undersampled diffraction tomography system as in the compressive sensing case), one should interpolate in Fourier Space and utilize nonlinear processing methods (e.g., compressive sensing) to achieve high quality reconstructions.

Interpolation in Fourier Space can be grouped into two principle types: grid-driven and data-driven interpolation. Grid-driven interpolation estimates the value at each grid point (in the case of tomography, the cartesian coordinates) based on

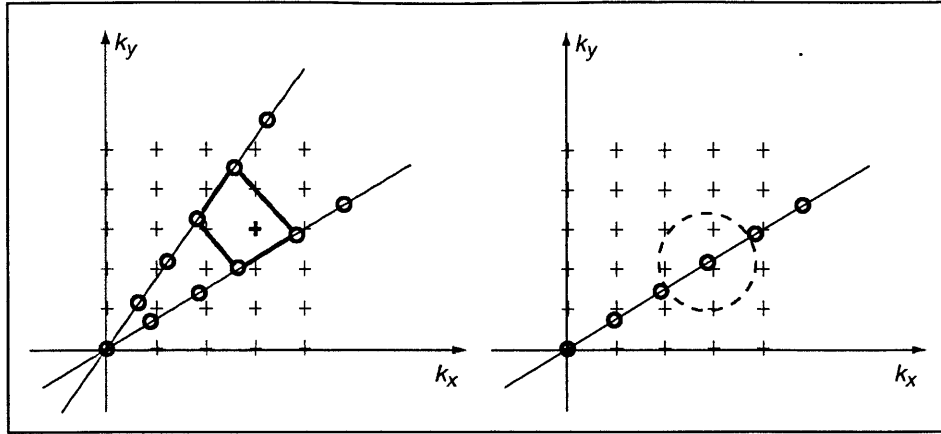


Figure 2-10: Grid-driven vs. Data-driven interpolation [14]

the surrounding known coordinates (from the actual measurements). A significant advantage of grid-driven interpolation is its simplicity (very easy to do e.g., bilinear interpolation, and it does not require a density estimate as data-driven interpolation does) when the location of the neighboring data points is known analytically. A disadvantage of grid-driven interpolation is that it will not, in general, use all of the acquired data for the reconstruction. (especially at locations where the collected data density is higher). As a result, it is not as SNR-efficient as data-driven interpolation.

In contrast, data-driven interpolation takes each each data point and add a weighted contribution from that point to a region of surrounding/neighboring grid points. Conceptually, one can think of this as convolving the collected data with a shift-variant kernel. This process “resamples” each measured pixel into the surrounding grid-points. The principal advantage of this method is that all of the collected data is used, and this method is thus more SNR-efficient than grid-driven approaches. The tradeoff is that in order to describe an accurate shift-variant kernel, one must decide on a density estimate to correct for the fact that the data may exist in greater concentration in specific k-space location. In the case of traditional tomography and diffraction tomography, these density weightings can be determined analytically, so the principle drawback to data-driven interpolation is actually processing speed. In general, the larger and more complex the interpolation kernel is, the slower the interpolation process will be.

2.2.6 Applications

In the optical regime, diffraction tomography has primarily been used for cell imaging. Feld et al have successfully imaged cells in 3D with high resolution using diffraction tomography coupled with phase unwrapping and iterative tomographic reconstruction techniques [15, 16, 17]. The advantages of the experimental system demonstrated in this work over interferometric DT systems (as well as other systems for deterministic phase retrieval) will be discussed later in this work.

Chapter 3

Phase Imaging & the Transport of Intensity Equation

Phase Imaging encapsulates the many broad and diverse methods used to image phase objects. An overview of different phase imaging methods are shown in Figure 3-1.

This section will discuss the first 3 (top row) of these imaging methods briefly and focus the remainder of the section on intensity-based phase retrieval.

3.1 Interferometric Phase Retrieval

Interferometric phase retrieval methods interfere the scattered wave passing through the phase object with a plane reference wave in order to generate a pattern of fringes that can be recorded on a camera. One could consider a Michelson interferometer used in such a simple manner to image the phase delay introduced by an object immersed in index-matching fluid.

As seen from figure 3-2, the image on the camera will be a pattern of fringes. Mathematically, the interference pattern observed is:

$$I(x, y) = |A_r e^{j\theta} + A_s e^{j\theta}|^2 \quad (3.1)$$

where A_r is the complex field from the reference arm of the interferometer and A_s is

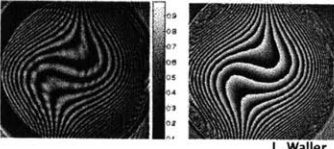
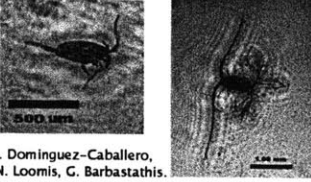
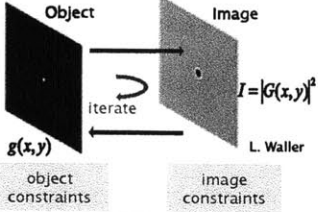

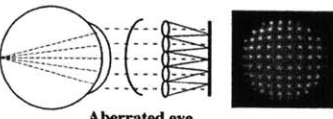
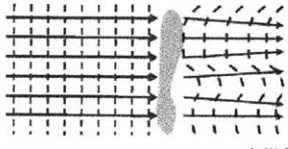
Interferometry	Digital holography (DH)	Iterative Phase Retrieval
<p>Requires coherent source, multiple phase-shifted images, unwrapping</p>  <p>L. Waller</p> $I = A_{obj}^2 + A_{ref}^2 + 2A_{obj}A_{ref} \cos(\varphi_{obj} - \varphi_{ref})$	<p>Interferometry + diffraction effects, Off-axis allows single-shot phase</p>  <p>J. Dominguez-Caballero, N. Loomis, G. Barbastathis.</p>	<p>Iterates between image spaces with corrections for a priori info</p>  <p>L. Waller</p> <p>object constraints image constraints</p>
DIC	Lenslet Arrays	Transport of Intensity
<p>Requires phase-shifted images</p>  <p>Nikon Microscopy U</p> $I = A_b^2 + A_s^2 - 2A_b A_s \cos(\Delta\varphi + 2\theta)$	<p>Does not require strict coherence, low spatial resolution</p>  <p>Aberrated eye</p> <p>University of Rochester</p>	<p>High-resolution, no unwrapping, no strict coherence requirements</p>  <p>L. Waller</p>

Figure 3-1: Overview of Different Methods for Phase-Retrieval

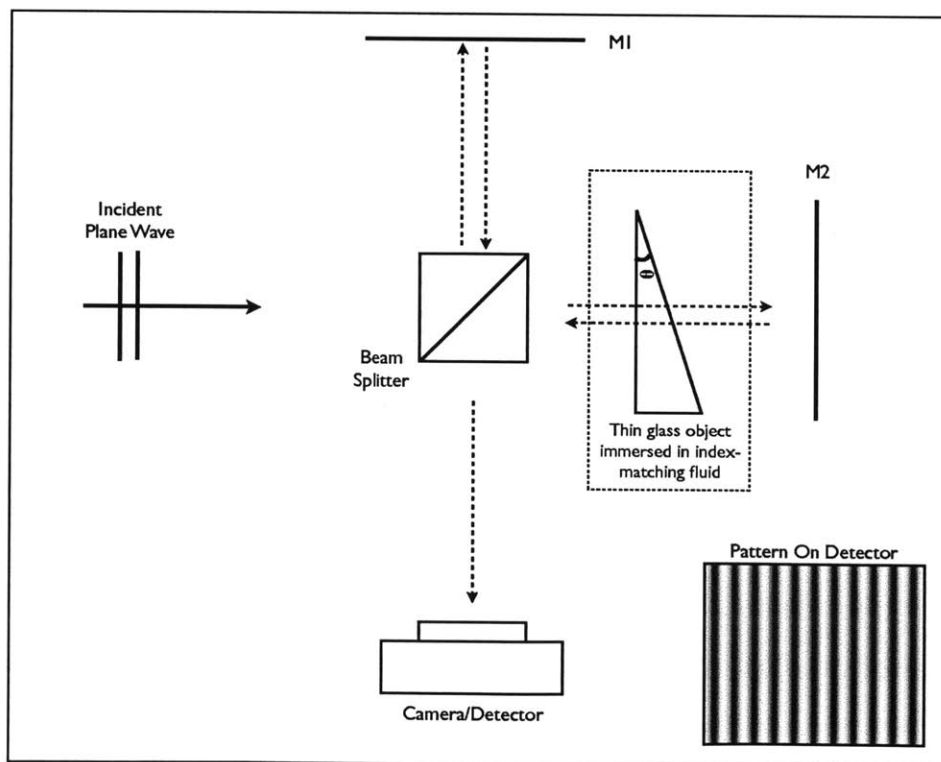


Figure 3-2: A Michelson Interferometer used to retrieve phase information from a pure-phase object.

the complex field from the signal arm (the arm where the phase object to be probed is. In order to tell from the existence of fringes that the object is tilted/slanted. By phase-shifting the reference arm at least twice by a small known amount (e.g., $\lambda/2$) and recording the intensities captured after each shift has been made, one can reconstruct the phase distribution after phase unwrapping to determine the direction of the tilt/slope of the object.

In order to abstract quantitative information about the phase of the object, these phase must be “unwrapped” [19, 20]. Phase unwrapping algorithms address the 2π phase ambiguity (e.g., a sudden jump by 2π in phase delay is not noticed in this interferometric system) issues as well as the directionality issue discussed earlier. The phase recorded on the camera ranges from $0 \rightarrow \pi$, so the total phase delay must be guessed based on how the phase is changing. Unfortunately, phase unwrapping is computationally challenging, and “jumps” in phase can lead to drastic errors in the phase unwrapping reconstruction. An additional drawback of interferometric systems is that they are typically complex, sensitive to noise/perturbations, and expensive to build/operate.

In order to capture 3-D phase information, either the object must be rotated or the imaging system must be rotated about the object. If images are acquired in such a fashion, then the object can be reconstructed three-dimensionally via principles of tomographic reconstruction discussed in chapter 2. In some cases, it is neither feasible to rotate the imaging setup (too bulky) nor the object (too small, as in the case of cells). In these cases, “partial-angle” tomography can be performed by scanning a beam through multiple angles (tilted plane wave) to illuminate different perspectives of the object. The fourier-space via this method is incomplete and resembles the same coverage one would achieve via synthetic aperture tomography.

3.2 Iterative Phase Retrieval

Iterative Phase Retrieval Methods begin with an initial guess for the phase of the object. That “guess” phase is forward propagated a distance z with a fresnel propa-

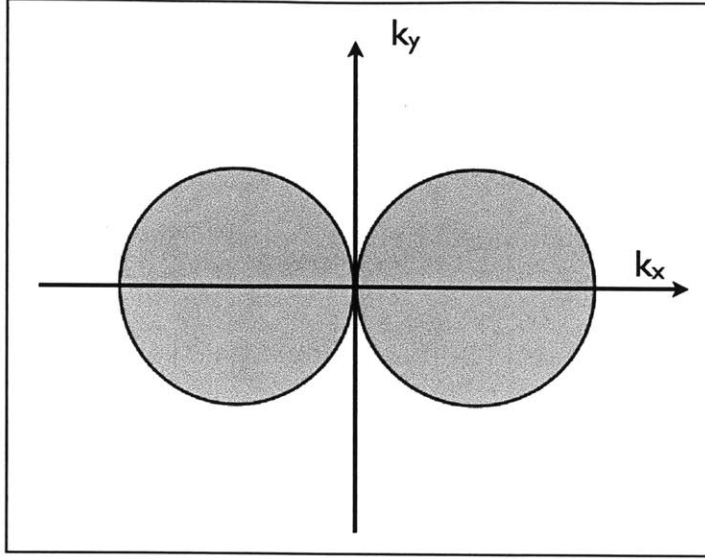


Figure 3-3: Fourier Space coverage of synthetic aperture tomography.

gation kernel [21]. The fresnel kernel, which can be thought of as a paraxial spherical wave with appropriate boundary conditions is given as:

$$h(x, y; z) = \frac{e^{jkz}}{j\lambda z} \exp \left\{ j\pi \frac{(x^2 + y^2)}{2z} \right\} \quad (3.2)$$

and thus the output field when the input field $g(x, y)$ is propagated by a distance z is given by:

$$g_{out}(x, y; z) = g_{in}(x, y) * h(x, y; z) = \mathcal{F} \{ G_{in}(u, v) * H(u, v; z) \} \quad (3.3)$$

The convolution can be computed as the superposition of weighted values of the inputs, or processed in the Fourier Domain (using, e.g., the FFT) for computational speed. The corresponding measured field at the output plane is given as:

$$I(x, y; z) = |g_{in}(x, y) * h(x, y; z)|^2 = |\mathcal{F} \{ G_{in}(u, v) * H(u, v; z) \}|^2 \quad (3.4)$$

The output intensity is then compared to the actual intensity output, and the constraint is then “back-propagated” to the input plane. Any input constraints known (e.g., the object is smooth, pure-phase, or has X pre-known features) are then

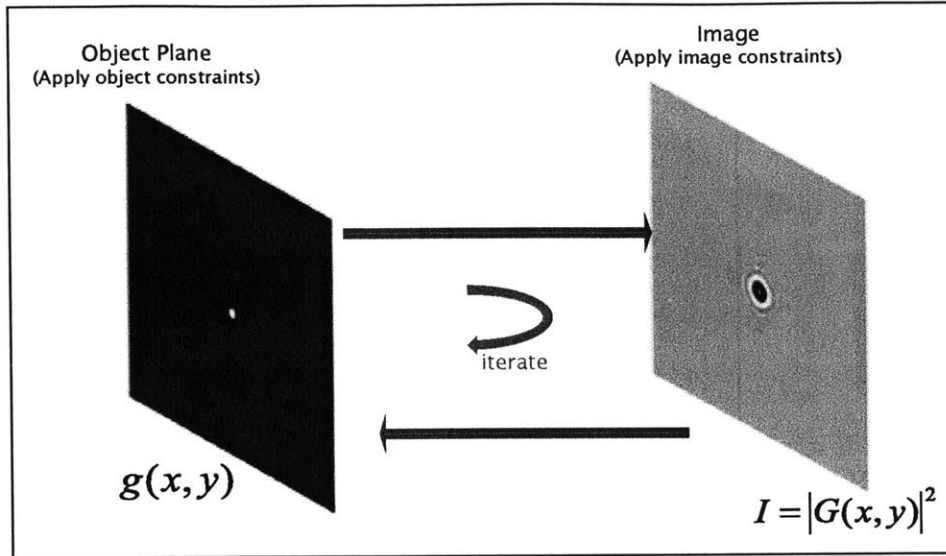


Figure 3-4: Iterative phase retrieval “ping-pongs” back and forth, applying constraints at the object and image planes, until a final answer is converged upon..

applied to this field, and the field is then re-propagated to the output plane. This process “ping-pongs” back-and-forth until a final solution is converged upon. One significant drawback of iterative phase retrieval methods is that their result is non-unique. Wedberg and Stamnes have previously demonstrated optical-regime phase tomography on a cylindrical object using this approach [65].

3.3 Digital Holography

The holographic inverse source problem seeks to determine the complete complex index distribution of three-dimensional (3D) objects from measured wavefront information. The procedure is difficult because inversion from intensity measurements to the scattering potential that generated that intensity is generally not a unique process. [22] Off-axis holography solves some of these issues but is experimentally more complex to setup. In-line holography is experimentally simple but requires extra computation for retrieval of object information.

Conventional methods to solve the holographic inverse source problem from in-line holograms use a two-step process. First, the hologram is back-propagated to

different transverse planes. Then, a focus metric is applied to the back-propagated images to remove out-of-focus content. The remaining in-focus features are explained to be the sources contributing to the original hologram. In general, the accuracy of these methods depend strongly on the effective use of a priori information in the filtering step. The theory of in-line digital holographic reconstruction is discussed more in chapter 4, when compressive sensing techniques are demonstrated as a tool for solving the holographic inverse problem of particle scattering.

3.4 Transport of Intensity

The general idea of transport of intensity imaging is that although a single intensity measurement cannot give you field information, if one know the intensity distribution of light as it propagates over an entire volume, then he can specify the field at all points within that volume exactly (in the absence of phase vortices).

When the field is paraxial, the TIE specifies the relationship between phase and the first derivative of intensity with respect to the optical axis, yielding a compact equation which allows direct recovery of phase information [8, 24]. Proof of the above equation (TIE) is in the appendix of this work. The TIE is valid for partially coherent illumination [23], allowing resolution out to the partially coherent diffraction limit and making it suitable for use in a brightfield microscope [27].

$$\frac{2\pi}{\lambda} \frac{\partial}{\partial z} I = -\nabla_{\perp} \cdot I \nabla_{\perp} \phi \quad (3.5)$$

In the above equation, I is the intensity measured in a plane perpendicular to the axis of propagation, z , and the \perp subscripts indicate the operator acting in a plane perpendicular to the optical axis. λ is the spectrally-weighted mean wavelength of illumination [23], and ϕ is the phase.

If the intensity is constant, then the previous equation reduces to a 2D Poisson Equation [29, 30].

$$\frac{2\pi}{\lambda} \frac{\partial}{\partial z} I = -\nabla_{\perp}^2 \phi \quad (3.6)$$

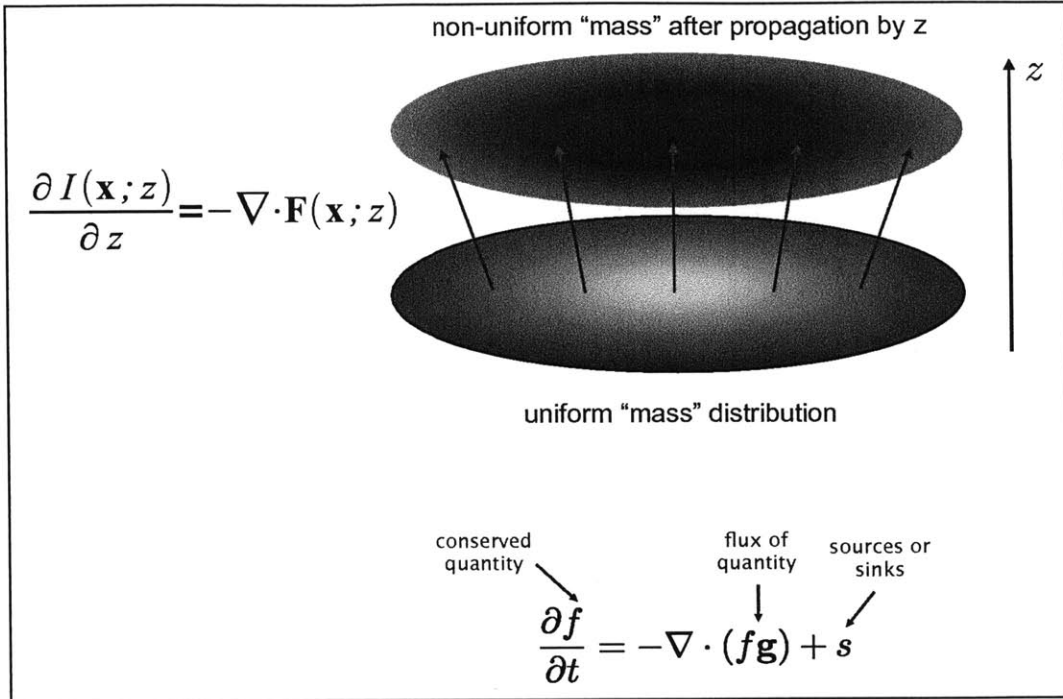


Figure 3-5: Transport of Intensity as conservation of mass

and can be solved using an FFT-based Fast Poisson Solver or via iterative algorithms. If the intensity is not constant, then a substitution must be made and the Poisson Equation solved twice to yield the retrieved amplitude and phase [8].

From a fluids perspective, the paraxial Transport of Intensity Equation (TIE) can be thought to describe flow due to a gradient potential. At its root, the TIE describes a conservational principle. The perpendicular gradient of the phase of coherent light represent the flux of light in/outwards in the x & y directions. The divergence of that quantity denotes the "source or sink" nature which arises due to the intensity change from plane-to-plane of constant z .

In the simulation below, a pure-phase "MIT" phase object is located at some distance away from the camera. By focusing at the plane where the object is, the camera will see nothing. If one defocuses the camera than he can see that an object is certainly present, but he/she has no idea what that object is. By applying the Transport of Intensity Equation, one can retrieve the exact value of the phase at the object plane.

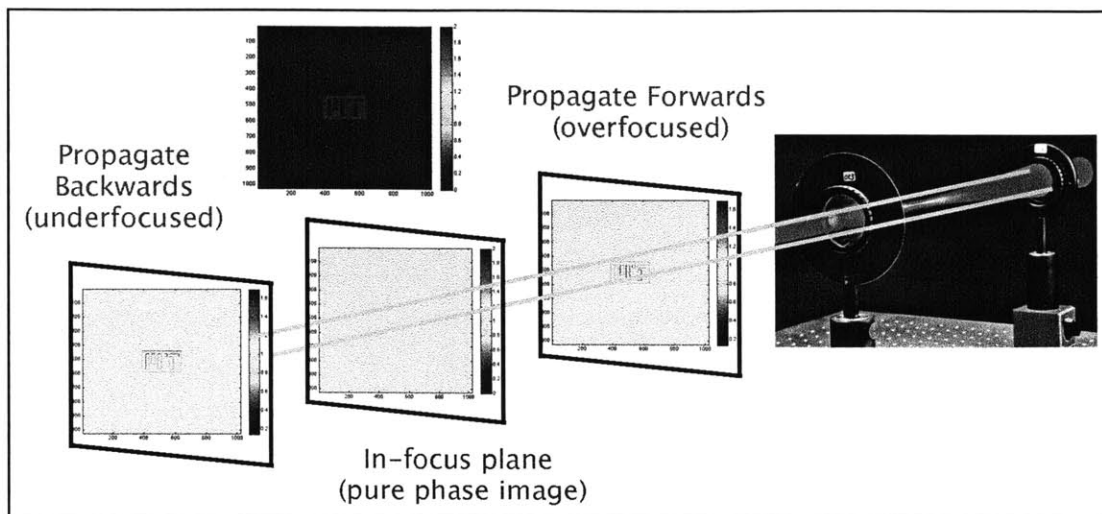


Figure 3-6: Transport of Intensity Simulation

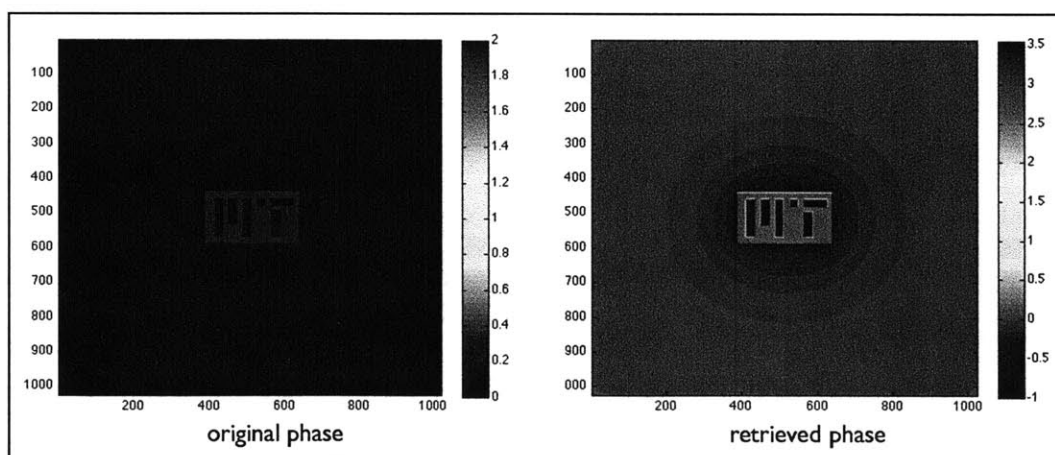


Figure 3-7: (Left) Original phase at input plane. (Right) Phase retrieved via application of TIE. Magnitudes of retrieved phase do not take into account scale factor in the data.

Chapter 4

Compressive Sensing

In the past decade, compressive sensing has emerged as a powerful tool for the systematic utilization of sparsity priors to improve estimates of solutions to underdetermined linear systems. Compressive sensing is optimal to use when measurements are “expensive” (costly in resources or time) and computational power (post-processing) is cheap/readily available.

Arising out of work on image compression, compressive sensing is premised upon the fact that a wide class of objects can be represented “sparsely” in some basis (e.g., wavelets). If the class of objects is known (e.g., you know the images will all be of blood vasculature), then a specialized dictionary or mixed basis can be trained and utilized for image reconstruction/denoising based on compressive sensing priors. In this manner, one can seemingly “break the Shannon-Nyquist” limit to resolution (because of the *a priori* knowledge that the object is sparse in a particular basis).

A significant problem with previous approaches utilizing sparsity priors was that in order to find the “sparsest” solution, a enormous space of the objective function needed to be searched. Essentially, the methods sought to minimize the L0 norm of inputs that would match the measured data (“sparsest solution possible”), a problem which Candes, Romberg, and Tao [31] proved to be NP-hard. Their solution to this problem was to, instead of seeking to minimize the L0 norm of the guessed solution, to seek to minimize the L1 norm instead (a problem solvable using linear programming techniques). This breakthrough, along with publicly accessible code for

solving underdetermined linear systems based on compressive sensing principles, has allowed the field of compressive sensing to flourish. In this chapter, I discuss and demonstrate the use of compressive sensing techniques for image reconstruction and for in-line digital holographic reconstruction.

4.1 Theory

Compressive sensing is a relatively recent non-linear sampling theory developed by Cands, Romberg, Tao, and Donoho [31, 32]. In contrast to the classical sampling theorems developed by Shannon and Golay in 1949 which posit that in order to accurately reconstruct a signal [33], the sampling rate must be greater than twice the spatial bandwidth, compressive sensing theory states that the number of samples required to accurately reconstruct a signal depends solely on the sparsity of the signal (i.e., the number of non-zero coefficients). In the context of compressive sensing, an S -sparse signal is one that has exactly S non-zero coefficients with all remaining coefficients having values of exactly zero. The number of samples required for exact reconstruction of a signal is related solely to the sparsity, S , of the signal, regardless of signal length or spatial bandwidth.

The authors in [31, 32, 34, 35, 36] have demonstrated that a signal, assumed to be sparse in a particular basis (e.g. space, wavelet, fourier, etc.), and sampled in an orthogonal domain can be accurately reconstructed with overwhelming probability using many fewer measurements than suggested by the Shannon-Nyquist sampling theorem. Recently, Takhar et al. applied compressive sampling principles to create a single pixel camera [37], and Brady et al. applied compressive sensing to reconstruct the scattering potential of dandelion seeds from in-line digital holographic measurements [56]. Candes and Plan [?] have shown that compressive sensing algorithms can be used in the presence of noisy measurements and function to denoise a signal (e.g., when the sensing matrix is identity matrix) both when the measurements are incomplete and when the measurement matrix is full-rank.

From basic linear algebra, it is known that at least n equations (or measurements)

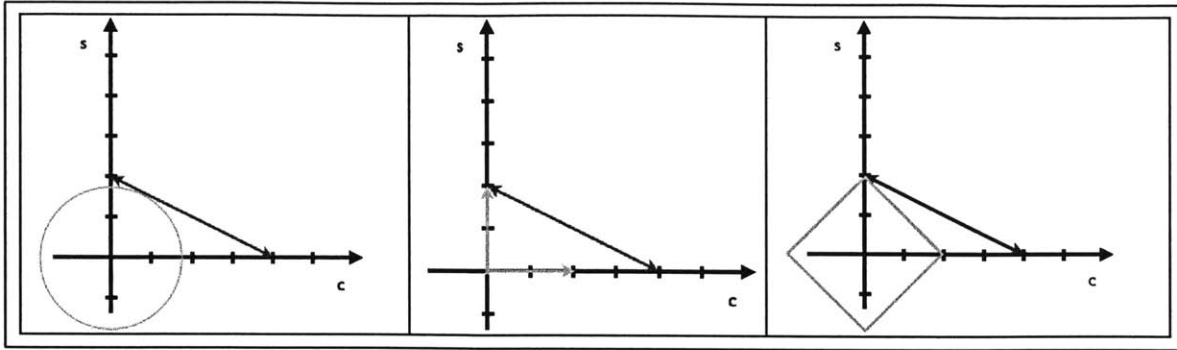


Figure 4-1: Compressive Sensing Reconstruction based on knowledge that an object is sparse in its L0-norm (majority of its coefficients are 0 in domain of interest) “grows” along the axes instead of minimizing the L2-norm (“growing a circle”). In practice, solving minimizing the L0-norm is NP-hard, so the L1-norm is minimized instead (“growing a diamond”).

are required to reconstruct a signal with n unknowns. If only m equations are given, where $m < n$, then the solution can be determined to be restricted to a line, plane, hyperspace, etc. The usual solution to determining an estimate for the signal of interest is to minimize the L2-norm (the sum of the squares of all of the coefficients; often associated with the energy of the signal) of the coefficients of the signal estimate. This is equivalent to growing a circle/hypersphere until it touches the line/plane/hyperspace of possible solutions. The first point of contact is the solution that minimizes the L2 norm of the estimate (while matching the observed measurements, which restrict data to a line/plane/hyperplane). If the signal is known to be sparse, then the appropriate solution should not seek to minimize the L2 norm, but instead should seek an estimate that minimizes the L0 norm of the signal. This is equivalent to searching along the axes for the first point of intersection.

Candes, Romberg, and Tao have proven that seeking a solution that minimizes the L0 norm is an NP-hard problem [31] and thus, infeasible for high-dimensional datasets. However, they also proved that if the sampling basis and measurements satisfy a sufficient condition called the restricted isometry property (RIP) [31], then seeking the estimate with a minimum L1-norm (the sum of the absolute values of the coefficients) converges to the same result as the estimate that minimizes the L0-norm

with overwhelming probability. Specifically, they proved that if:

$$m \geq |S| \cdot \mu^2(\Phi, \Psi) \cdot \log(n/\delta) \quad (4.1)$$

where m is the number of measurements, S is the number of non-zero coefficients in the signal, n is the length of the signal, and μ is the degree of coherence between the signal and measurement bases (i.e., the maximum inner product between the two bases; equal to 1 for orthogonal bases), then the L1-norm retrieves the same result as the L0-norm with probability $P > (1 - \delta)$

The conclusion found was significant because L1-minimization problems can be solved rapidly with linear programming methods. Variations of the L1-minimization problem (such as Total Variation (TV) minimization, which minimizes the L1-norm of the gradient of an image) can be cast as Second-Order Cone Problems and solved in related manners.

Various open-source L1 and TV-minimization solvers are readily available, and we adapt the compressive sensing solvers NESTA (developed by Becker, Bobin, and Cands) [39] and TwIST (developed by Bioucas-Dias and Figueiredo) [40] towards the applications of image restoration and compressive holography demonstrated later in this chapter.

4.2 Applications

4.2.1 Incomplete Fourier Measurements

A common orthogonal domain to take measurements in (or to have measurements analyzed in) is the Fourier Domain. Many interesting discrete-time signals are sparse in the time domain, and many others are sparse in frequency (e.g., people's voices or the sounds that a machine can make are often limited in frequencies that they can emit). In the optical regime, measurements taken at the pupil plane of a $4f$ system are the Fourier Transform of the input. If a signal is sparse in the time domain, then it is optimal to take measurements in the Fourier Domain (or any other orthogonal

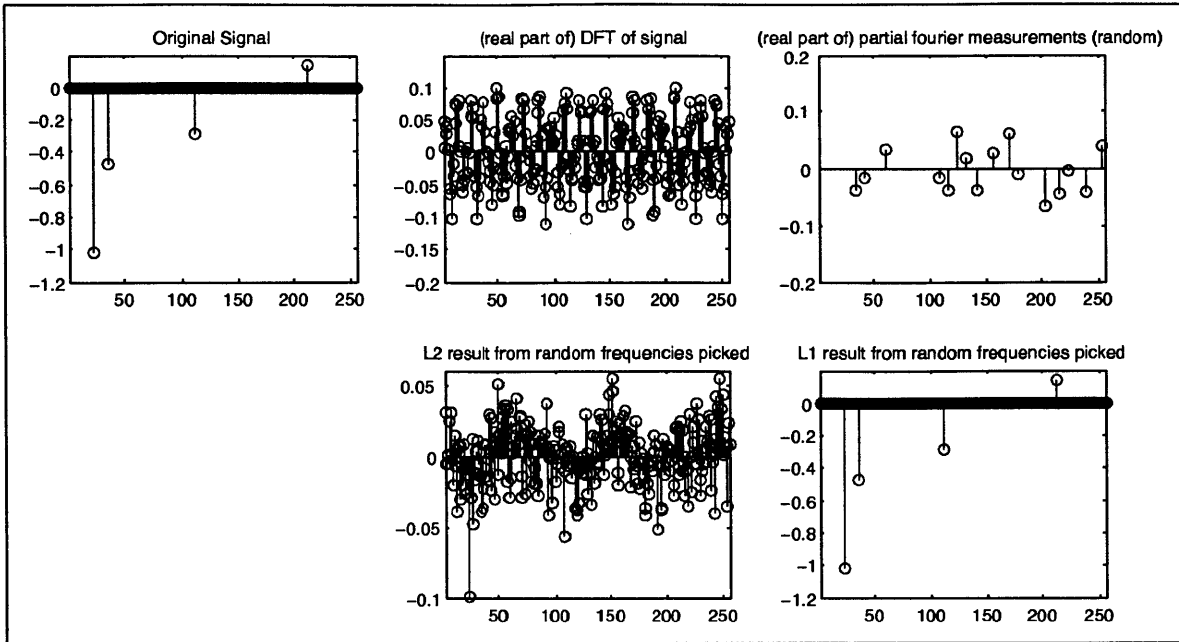


Figure 4-2: Compressive reconstruction of sparse signal from limited number of random Fourier-Domain measurements.

domain). If a signal is sparse in the frequency domain, then it is optimal to take measurements in the Time/Space Domain (or any other orthogonal domain). From a limited subset of measurements in an orthogonal domain, sparse signals can be reconstructed exactly using principles of compressive sensing.

Figure 4-2 demonstrates compressive sensing results when the samples in the orthogonal domain are selected randomly. As mentioned earlier, the authors in [35] proved that random measurements are optimal for gleaning maximal information from the orthogonal domain from as few measurements as possible.

In some cases, one cannot take random measurements in an orthogonal domain. For instance, optical systems are limited by aperture size and their output are low-pass filtered (only lower spatial frequencies that pass through the aperture). This means that the “sampled” frequencies all lie within a low-frequency region (they are not randomly selected). Figure 4-3 illustrates that even though this is the case, it may still be possible to reconstruct a result from the low-pass-filtered/undersampled data using CS principles that is accurate when compared to the original signal. This is, in a sense, a form of “super-resolution” achieved computationally by applying the

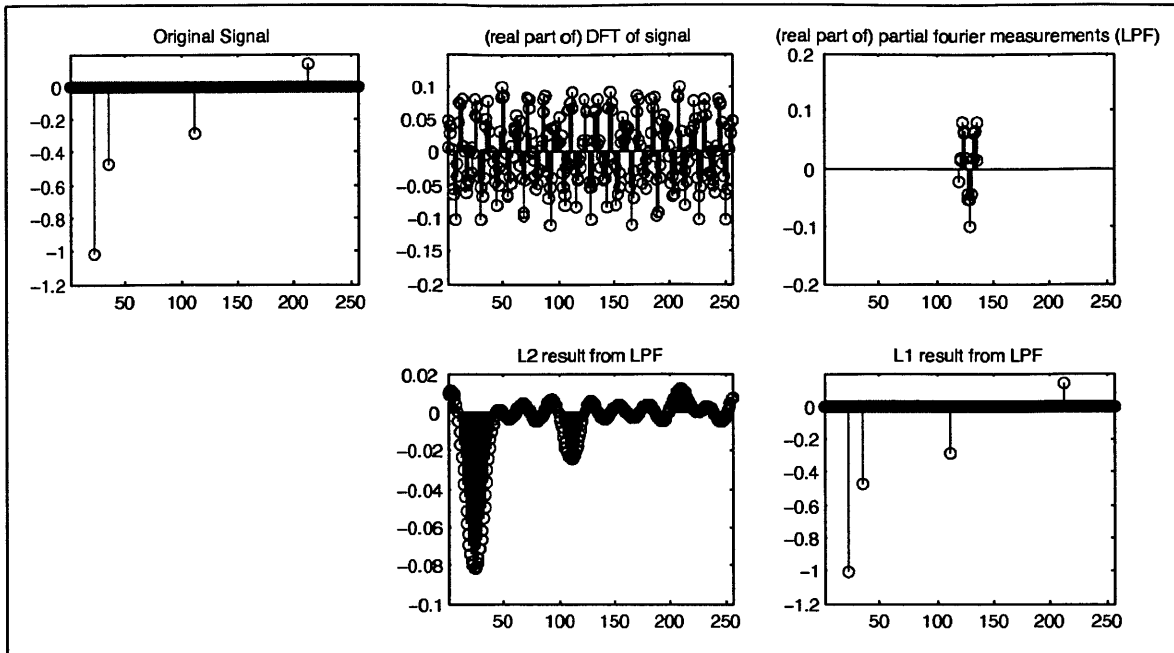


Figure 4-3: Compressive reconstruction of sparse signal from low-frequency Fourier-Domain measurements

extra knowledge that the object to image is sparse (or sparse in its gradient or in some other domain, as discussed later) towards the reconstruction of the original signal.

Compressive reconstruction methods work not always work if the samples are not randomly chosen. For instance, one can imagine if the input were a single delta function and the measurements were taken periodically. It would be possible for the measurements to hit all zeros, thus providing no information to the user at all. The “super-resolution” discussed earlier is also problematic when the signal is not locally sparse (if the signal is composed of thin rectangles instead of just spaced-out spikes). Taking measurements randomly in an orthogonal basis avoids these issues.

The results in Figure 4-2 and 4-3 hold even in the presence of noise (although they require more measurements for accuracy), which is better than simple deconvolution could do. A general rule of thumb is that one must have approximately “ $4 \cdot S$ ” measurements (in an orthogonal domain to the domain that the signal is sparse in) in order to reconstruct an S -sparse signal exactly.

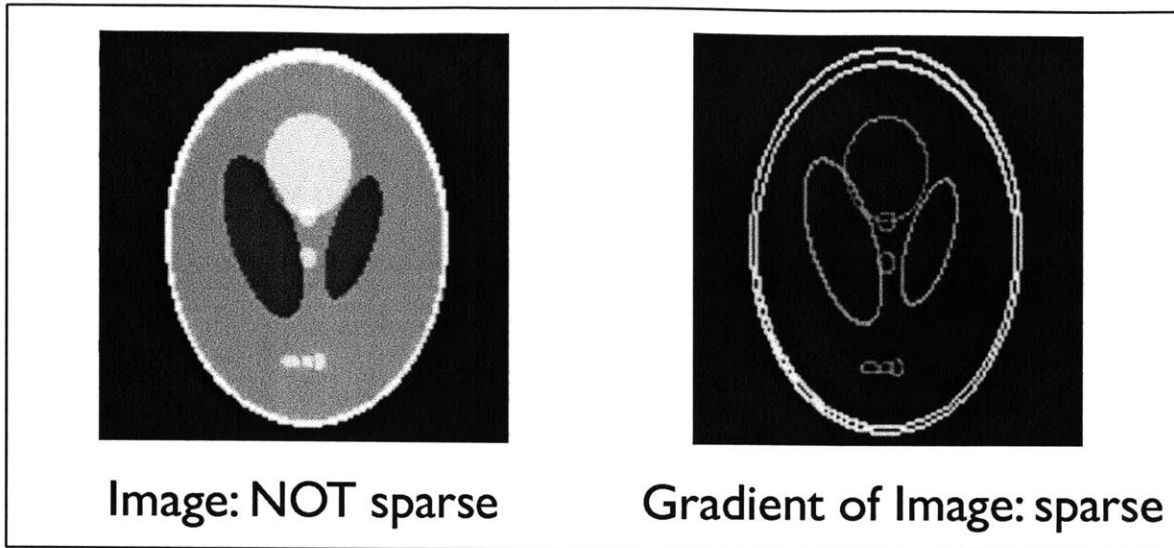


Figure 4-4: Even when the object itself is not sparse, compressive sensing methods may still work by minimizing some other norm such as the Total Variation Norm (L1 of the gradient of the image). An overwhelming majority of objects man-made/nature-made are “smooth” (sparse in wavelet domain and TV norm) and will not correlate with noise.

4.2.2 Compressive Tomography

The Fourier-domain demonstrations of compressive sensing shown in the previous subsection easily extend to 2-Dimensional signals, and the extension invites the logical next-step of using compressive sensing to improve tomographic inversion, which by nature is an incomplete sampling problem (discussed in chapter 2).

Since most real-world object aren't sparse (i.e., they're not composed of dots), a different domain is used for compressive tomography techniques. In general, instead of minimizing the L1-norm of the object in the space domain, either (1) the L1-norm in the wavelet domain (or a trained dictionary domain) or (2) the TV-norm (L1-norm of the gradient of the image) in the space domain is minimized. The TV-norm is assumed to be sparse since the features of an image are assumed to be “mostly smooth” across the image, without many abrupt large changes.

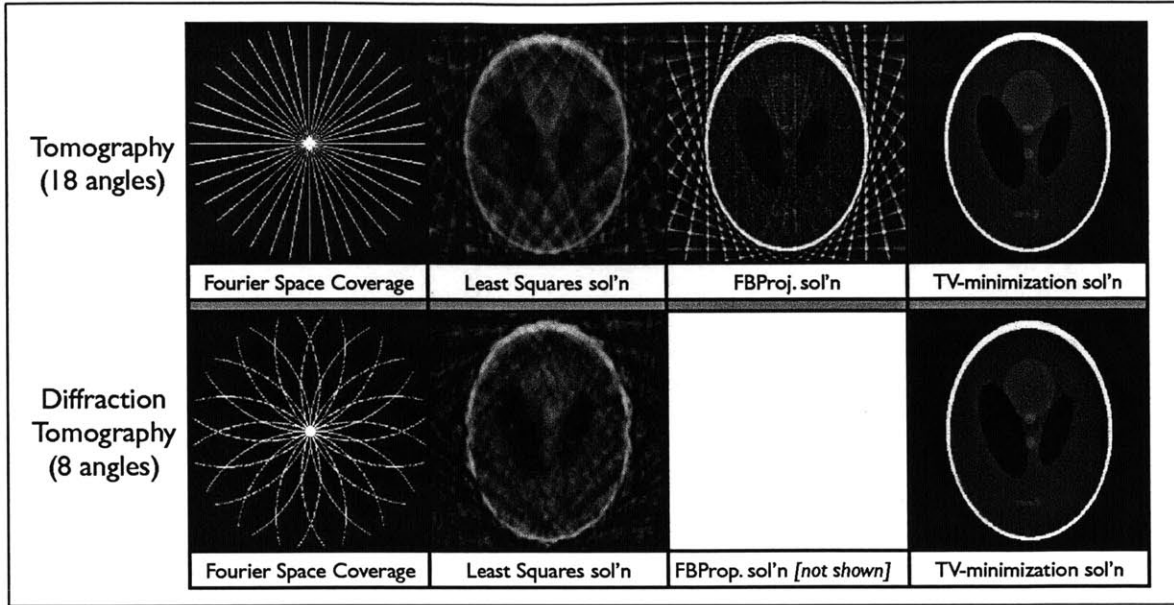


Figure 4-5: Compressive Sensing can be used for exact tomographic reconstruction from a limited number of angles of projection

4.2.3 Image Restoration

In the above sections, we considered that the signal was sparse in space (or total variation) and that the samples were acquired in a domain orthogonal to the space domain. This sequence need not be in this order, and it is possible to consider *measurements* occurring as samples of the space domain and the compressive sensing solver solving for a solution in an orthogonal domain (e.g., wavelet) which is sparsest (or has the lowest L1 norm possible). This is the case for compressive-sensing based image restoration techniques. The “incomplete measurements” are the subset of pixels of the image acquired, and the “signal” is the wavelet-domain representation of the image.

Applying compressive reconstruction principles in reverse allows one to accurately reconstruct images from a vastly smaller-than-100-percent subset of actually measured pixels. The ratio of pixels required for perfect reconstruction can be lower than 10 percent for CS techniques based on trained dictionaries. The compressive results shown in the figure have much lower L2 error than if the gaps in the images were simply reconstructed using bilinear interpolation (comparison shown in appendix).

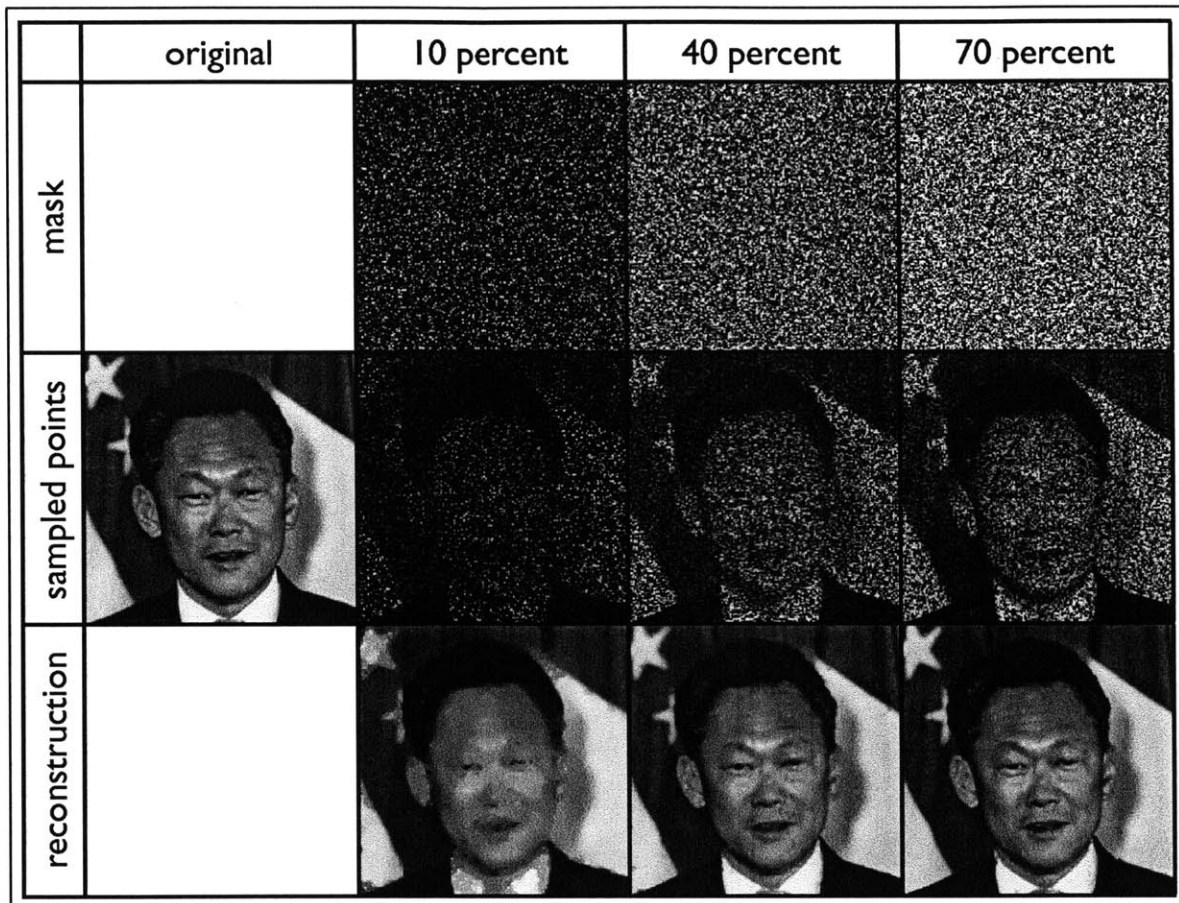


Figure 4-6: Compressive Sensing can be used to reconstruct an image based on a tiny subset of pixels. The reconstruction adds the *a priori* information that the image is smooth. Reconstruction quality can be improved if the image is known/assumed to be sparse in a particular tailored dictionary domain.

4.3 Compressive Digital Holography

4.3.1 Theory

In-line Digital Holography provides an experimentally simple setup for imaging in 3-dimensions and has been used widely for underwater marine biological research (e.g., imaging of plankton movement), particle image velocimetry (PIV), and biological microscopy [41, 42, 43]. A typical Gabor-type (in-line) digital hologram captures single-shot images recording the interference pattern between an on-axis reference plane wave and the scattered field from a collection of objects. After the image is captured, numerical methods are used to reconstruct the scattering potential of the object(s) of interest (i.e., those that generated the scattered fields which interfere with the reference wave to form the interference pattern captured on camera) [44, 45]. In-line digital holography suffers from the twin-image problem [46], and resolution is limited by the detector size. As a result, the quality of reconstructions obtained from on-axis digital holography is usually quite poor.

The simplest possible digital holographic setup involves illumination of a scattering object (or set of objects) with a spatially coherent, monochromatic plane wave. A Gabor (in-line) hologram is formed by the interference pattern of the original wave, E_r , with the wavefront generated by the illuminated objects with scattering potential $\eta(x', y', z')$. Since cameras can only record intensity at optical frequencies, a 2-D detector array records the irradiance incident on the camera:

$$I(x, y) = |E_r + E_s|^2 = |E_r|^2 + |E_s(x, y)|^2 + (E_r^*)(E(x, y)) + (E_r)(E^*(x, y)) \quad (4.2)$$

Under the first order Born approximation (valid for small, weakly scattering objects), each point within the scattering object is assumed to scatter just once, and the scattered field, E_s , is given by:

$$E_s(x, y) = \int \int \int dx' dy' dz' \eta(x', y', z') h(x - x', y - y', z - z') \quad (4.3)$$

where $h(x, y, z)$ is the Fresnel kernel, which designates the free-space propagation of a point- source [18].

For a planar reference wave, the term $|E_r|^2$ is constant, and thus it can be removed by subtracting the DC term from the Fourier Transform of the measured intensity. Additionally, E_r can be assumed to be equal to 1 without loss of generality. Then, the above equation for irradiance reduces to:

$$I(x, y) = 2\text{Re} \{E_s(x, y)\} + |E_s(x, y)|^2 \quad (4.4)$$

Folding the nonlinearity cause by the $|E_s(x, y)|^2$ term into a term for model error, $e(x, y)$ results in the equation:

$$I(x, y) = 2\text{Re} \{E_s(x, y)\} + e(x, y) \quad (4.5)$$

The equation above represents a linear mapping between the scattered field and measurement intensity.

Brady et al. showed that by combining the first Born approximation with a multi-slice approximation, the discretized field at the detector plane (i.e. upon each pixel of the camera) is given by [56]:

$$E_{n_1, n_2} = \mathcal{F}_{2D}^{-1} \left\{ \sum_l \hat{\eta}_{m_1, m_2, l} \exp \left\{ jkl\Delta_z \sqrt{k^2 - m_1^2 \Delta_k^2 - m_2^2 \Delta_k^2} \right\} \right\} \quad (4.6)$$

where $\hat{\eta}$ denotes the Fourier transform of η , \mathcal{F}^{-1} denotes the discrete inverse Fourier Transform operator, Δ_k denotes the lateral sample spacing (pixel size/lateral resolution), and Δ_z denotes the sample pitch in the z-axis (depth resolution). By letting:

$$\bar{g} = G_{2D} Q B f \quad (4.7)$$

where B is a block-diagonal matrix of 2D DFT's of size N_x by N_y and $Q = [P_1 P_2 \dots P_{N_z}]$ representing slice-by-slice propagation. $\left([P_l]_{m_1, m_2} = e^{jkl\Delta_z} e^{jl\Delta_z \sqrt{k^2 - m_1^2 \Delta_k^2 - m_2^2 \Delta_k^2}} \right)$

As discussed earlier, the squared field term can be folded into the error term, and doing so allows an in-line holographic intensity measurement (under First-order Born and multi-slice approximations) to be algebraically written as:

$$g = 2\text{Re}(\bar{g}) = 2\text{Re}\{G_{2D}QBD\} + e \quad (4.8)$$

The above equation expresses a linear relationship between the scattering potential, f , and the observed intensity, g . The error term, e , is comprised of components due to ignoring the nonlinear term of the squared field and components due to system noise. The nonlinear error is traditionally removed using off-axis holography, but Brady et al. showed that the denoising properties of compressive sensing can be used to localize the error generated by the nonlinear term to the reconstruction slices closest to the detector plane or to remove the error altogether [56]. Ignoring noise for now, and casting the above equation as $Ax = b$, the optimization problem can be defined as follows:

$$\text{Minimize } \|x\|_{\text{objective function}} \text{ subject to } \|b - Ax\|_{l_2} \leq \epsilon \quad (4.9)$$

The goal is to find the scattering potential, f , with the best objective function fit (e.g., lowest L1-norm or TV-norm) that matches the observed data (i.e. the recorded hologram, g) to within a maximum level of error tolerance, ϵ . Several open-source compressive-sensing solvers have been written to solve problems framed in such a manner, and we adapt the solvers “NESTA” and “TwIST” [39, 40] to solve the optimization problem.

4.3.2 Experiment

An in-line digital holographic imaging system was set up to image particles moving in water. A spatially filtered and collimated reference beam from a 633nm HeNe laser was used to illuminate a fish-tank filled with distilled water and seeded with microparticles. In order to satisfy conditions of compressive sensing and the first-order Born Approximation, the particles were seeded at a sufficiently sparse density.

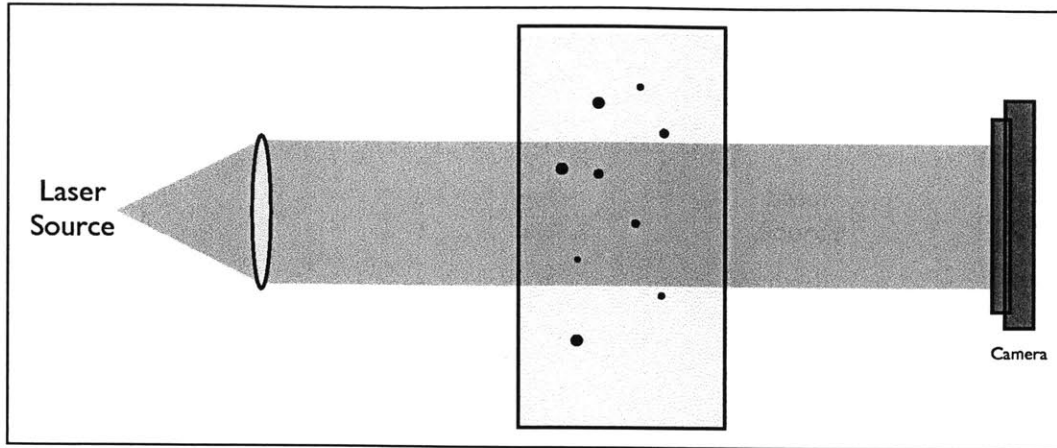


Figure 4-7: In-line digital holography setup

Images were captured on a 2592-by-1944 pixel Aptina MT9P031—12STM CMOS camera. After capture, the images were downsized (cropped) to 200 x 200 pixels for ease of computation and zero-padded on all four sides to a size of 512 x 512 pixels in order to avoid artifacts caused by circular convolution from use of the Discrete FT/FFT. Data processing was performed on a laptop with a 2.66GHz Intel Core i7 processor with 8GB of RAM. The codes used to process the data were written in Matlab, and the processing took about an hour.

The compressive sensing method was able to reconstruct three-dimensional scattering potentials and determine the 3-dimensional locations of the particles (shown below). By repeatedly running the algorithm for multiple frames of image capture, a video tracking the 3-dimensional movement of each particle was generated (not shown).

As discussed by the authors in [56], because the diffraction patterns generated by the squared field term don't correlate well with all of the object planes, the noise created by ignoring this term in the linearizing formulation used in this paper tends to remain localized within the first few planes of reconstruction. By segmenting out these planes of noise (which can be safely assumed to be devoid of scattering potential as per the setup geometry) we may overcome errors introduced into reconstruction from in-line digital holography due to the nonlinear squared scattered field term.

To remove the effects of the twin image on the reconstruction, we numerically

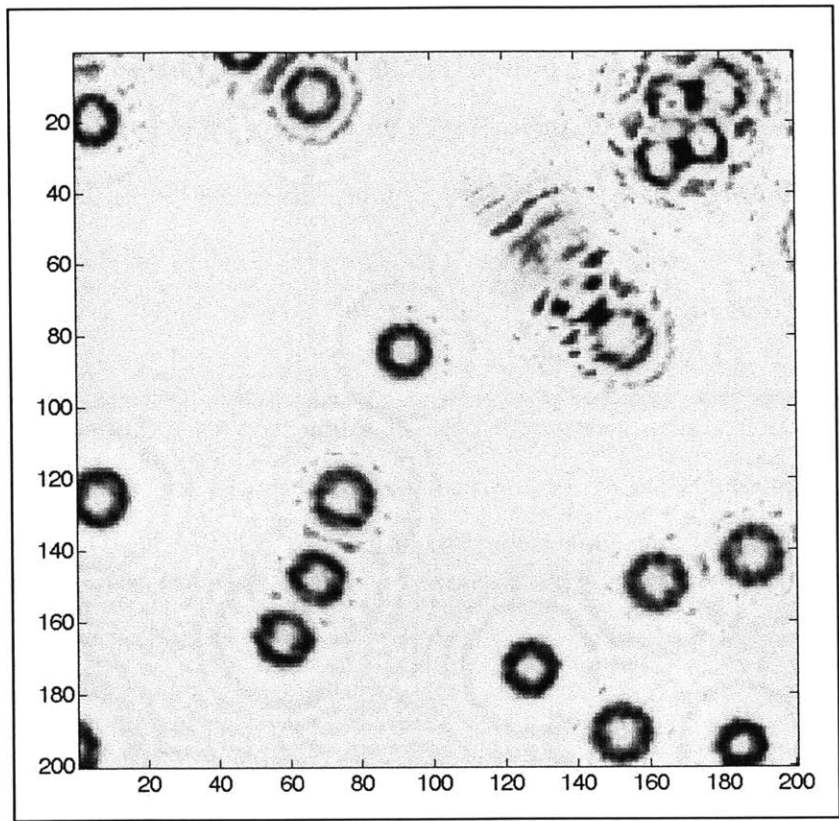


Figure 4-8: Digital Hologram of bubbles images with the setup in the preceding figure

confine our estimate domain to just one side of the measurement plane. The “optimization problem” we define for our compressive holography experiment solves for the 3D scattering potential of the object rather than a field at any particular position (which require calculation of a superposition of all of the object planes, each of which is at a different distance away), and by picking an object/ scattering potential, η , on one side of the measurement plane, we know that the virtual object, η^* , will be located on the other side of the measurement plane. Thus, by confining the reconstruction domain to just one side of the captured hologram, we can readily resolve the twin image problem in the reconstruction. A similar line of logic was successfully applied by Latychevskaia and Fink to remove the twin image problem in 2D digital holographic reconstruction [47].

Classically, the transverse resolution of an imaging system is given by: $\Delta x \sim \lambda z/D$, where z is the distance from the object, and D is the aperture size. Axial resolution is given by $\Delta z \sim \lambda(2z)^2/D^2$. However, by using non-linear compressive sensing theory, we are able to overcome these resolution limits.

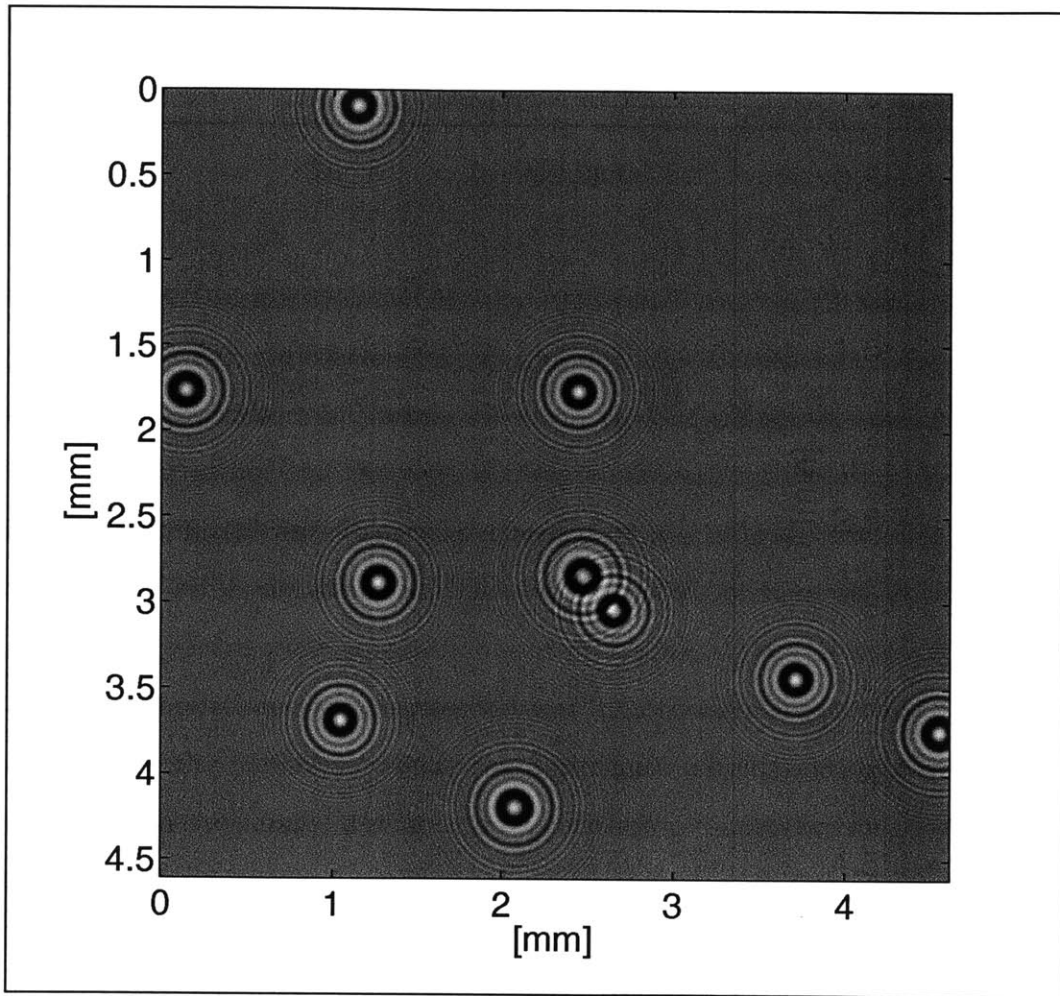


Figure 4-9: Simulated Hologram with 10 particles at different z depths

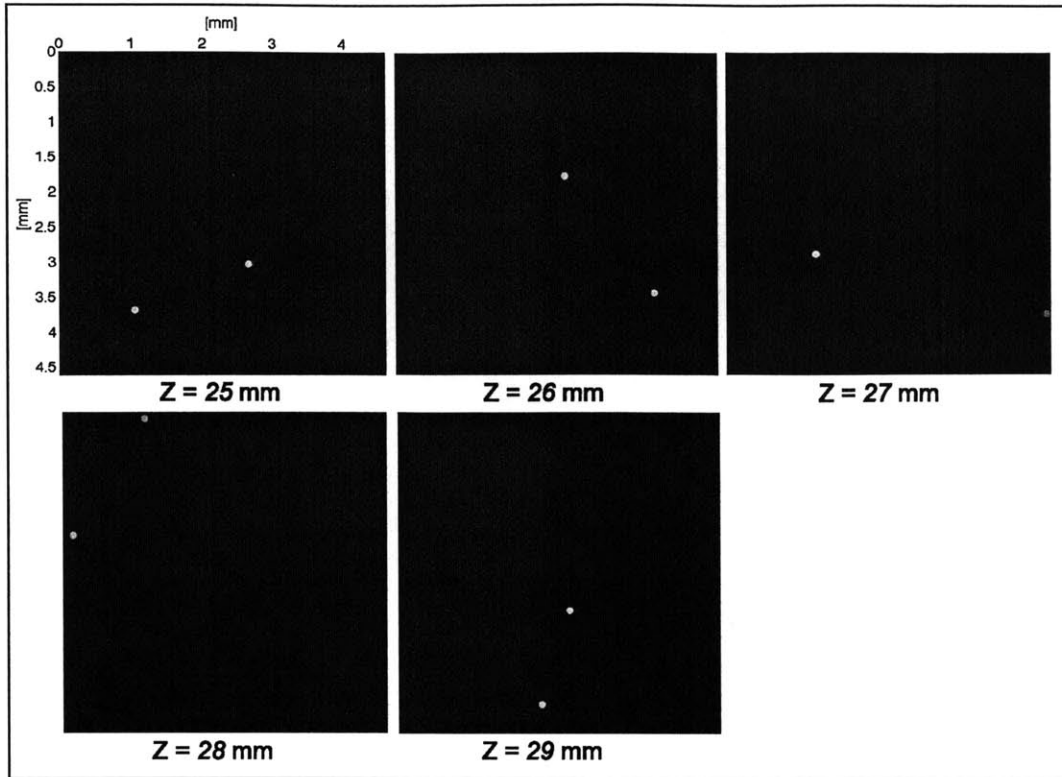


Figure 4-10: Compressive Reconstruction of several planes of the volume from simulated hologram. Bubbles show localization to the correct plane.

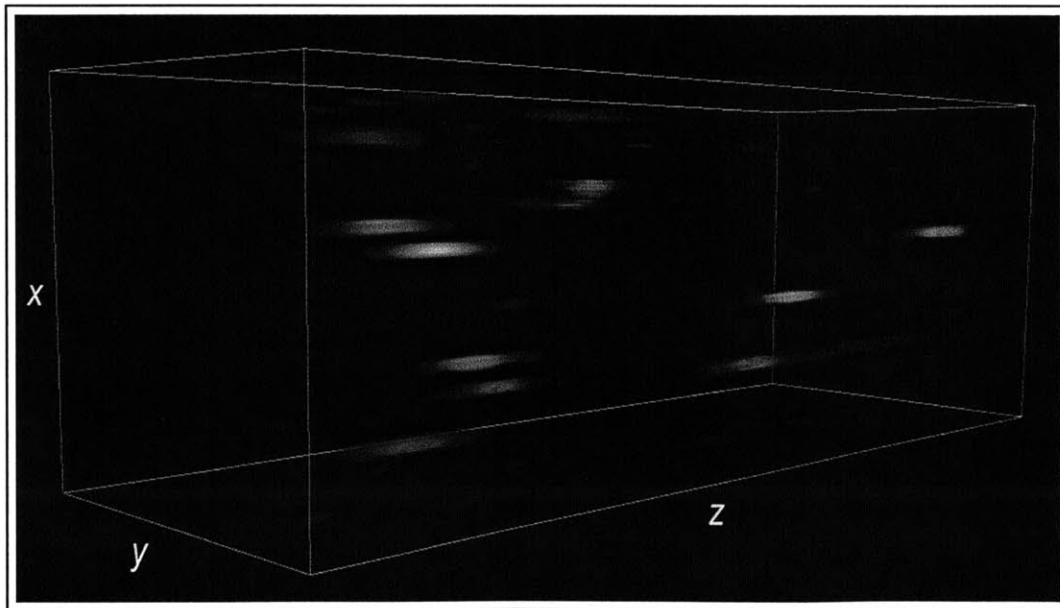


Figure 4-11: Volume-rendered Compressive Reconstruction of entire volume of recorded hologram from Figure 4-8

Chapter 5

Intensity-Based Phase Tomography

This section presents the principal contribution of this thesis. A bulk phase object is imaged tomographically, and the 3-dimensional profile of that object is reconstructed using principles of intensity transport and diffraction tomographic reconstruction. Results from direct inversion without application of transport intensity, and direct inverse using an inverse radon transformation are also shown as well. In the case of the former (reconstruction without application of TIE), results were very poor. In the case of the latter (reconstruction without consideration of diffraction), results match actual physical characteristics of the diamond fairly well. The reconstruction fidelity can be improved by taking diffraction effects into consideration, and the ability to improve results even further from use of compressive sensing is discussed and simulated.

5.1 Background/Motivation

Phase contrast microscopy is the traditional method for qualitative imaging of weak phase objects (those with indices of refraction close to that of their surrounding media). If quantitative results are desired, as is often true in the case of cell imaging within the fields of pathology and cell biology, then interferometric systems coupled with the use of phase unwrapping algorithms are usually employed to quantify the amplitude and phase of the field observed at a detector plane. If the complete three-dimensional (3D) structure of the phase object is desired, then the data is acquired to-

mographically and inversion algorithms are used to reconstruct the three-dimensional complex index distribution of the object.

Unfortunately, interferometric measurement systems are often bulky, expensive, and sensitive to small perturbations. Furthermore, phase unwrapping requires sophisticated post-processing that is generally unstable with noise, introducing reconstruction artifacts. Intensity-based phase retrieval techniques, in which both the amplitude and phase of a field are retrieved from defocused intensity measurements, offer an experimentally simple solution to determining phase quantitatively without the use of phase unwrapping algorithms.

Recently, it has been shown that transport of intensity can be used to image optical fibers (cylindrically symmetric) immersed in index-matching fluid [26]. In this chapter, we apply transport of intensity principles to tomographically image and reconstruct an asymmetric bulk phase object (12 mm thick) in 3D. My imaging system, which is capable of retrieving the complex index distribution of a phase object without use of interferometry, has wide applicability in fields such as underwater imaging, cell biology, pathology, and even x-ray imaging (e.g., for security or medicine). An added benefit is that our system is experimentally simple to set up and can be easily adapted to fit imaging geometries of conventional brightfield microscopy with minimal modifications.

Intensity-based methods of phase retrieval are based upon the principle of conservation of energy of a propagating wavefield. The transport of Intensity Equation, upon which TIE tomography and Intensity Diffraction Tomography (IDT) are based, is discussed in Chapter 4. If multiple projection angles about an object are captured, then the objects complex index distribution can be reconstructed by following basic principles of tomography [4, 6]. For my tomographic setup, I chose to rotate the object inside the imaging system rather than the system about the object for reasons of experimental simplicity.

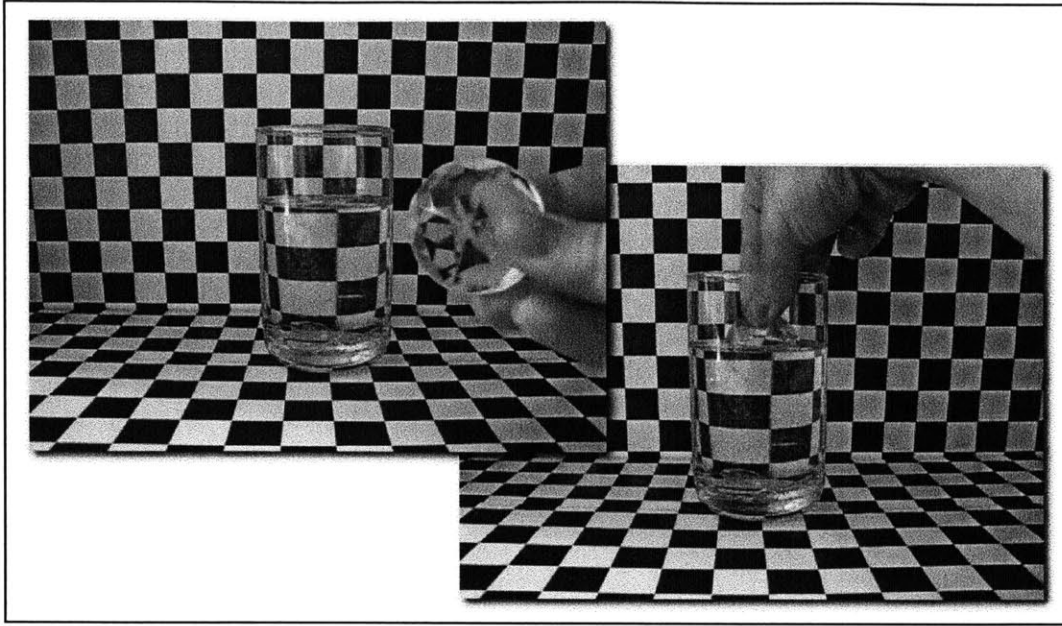


Figure 5-1: A glass diamond index-matched to its surrounding media was used for this experiment. Placing the diamond in the oil turns it “invisible” to our eyes (it delays light passing through it but does not alter its amplitude/intensity)

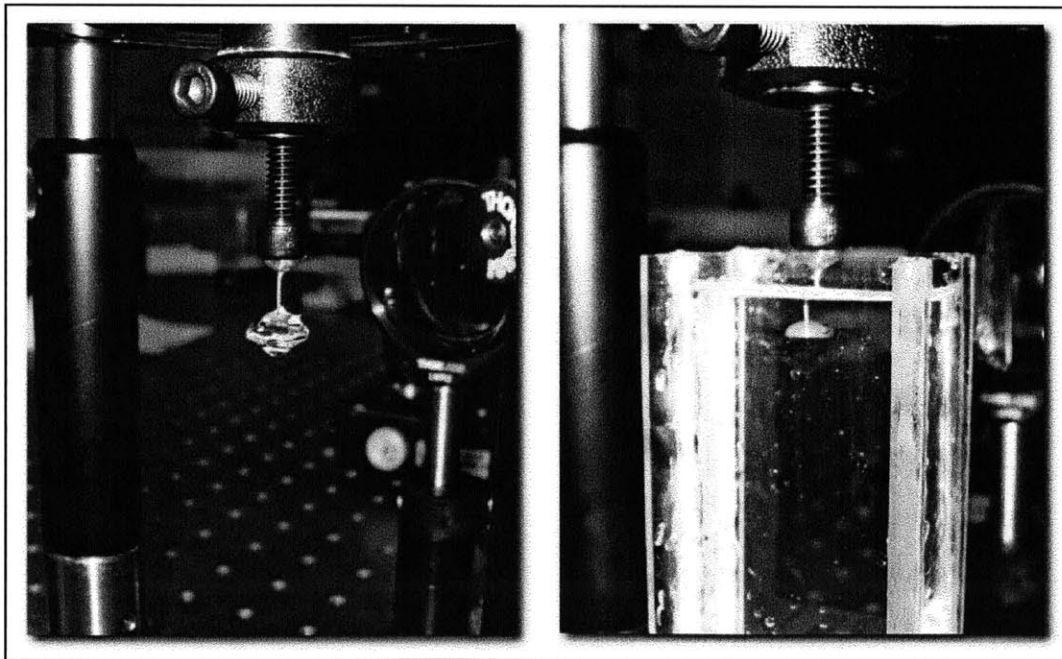


Figure 5-2: A smaller version of the diamond in the preceding figure was used for this experiment. The diamond was mounted on an inverted rotation stage so that images could be acquired in a tomographic fashion.

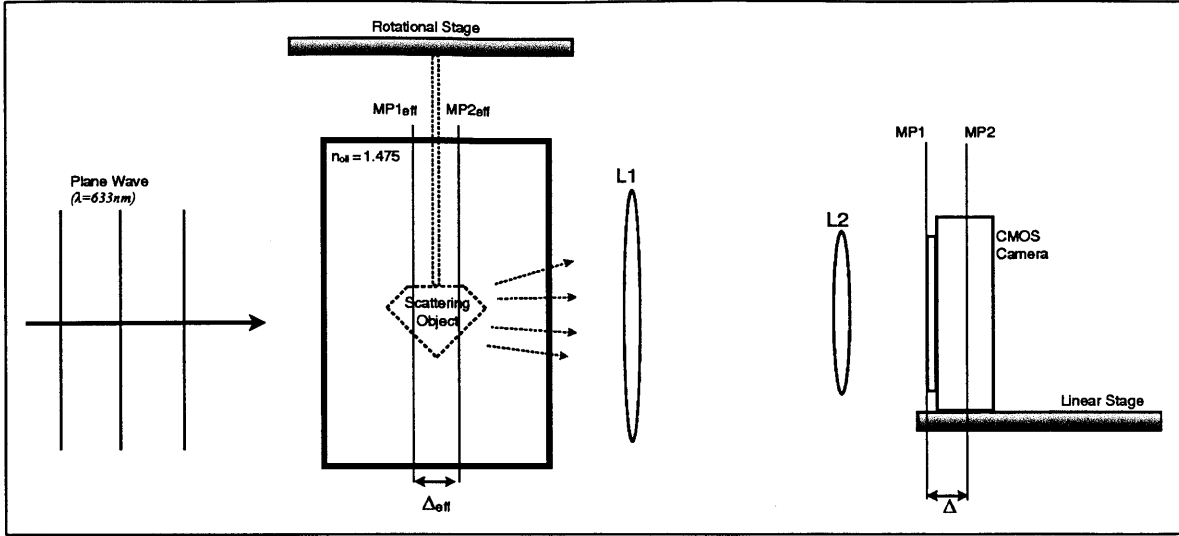


Figure 5-3: Experimental Setup

5.2 Experiment: Diffractionless Assumption

A transparent object (Pyrex diamond) was placed in index-matching fluid and imaged using the system in Figure 5-3. The experimental setup consisted of a rotation stage mounted in an inverted position to hold the scattering object suspended in index-matching medium. A $4f$ (4x demagnification) imaging system was used to center defocus about the object and to relay the image onto the camera detector (Aptina CMOS) which was mounted on a linear stage.

The object was illuminated with a collimated plane wave from a 632.8nm HeNe laser. Intensity measurements were taken from 90 independent and equally spaced angles through a total of 180° of rotation (Figure 5-3). Since the imaging system could not be easily rotated, the object was rotated 2° between each set of image captures. At each angle, three images were taken: one corresponding to the in-focus image of the object, one corresponding to an over-focused image of the object via movement of the linear stage by $+10\mu m$, and one corresponding to under-focused images of the object obtained from movement of the linear stage by $-10\mu m$. The $\pm 10\mu m$ defocus images were used to generate tomographic reconstructions using TIE tomography and using IDT methods.

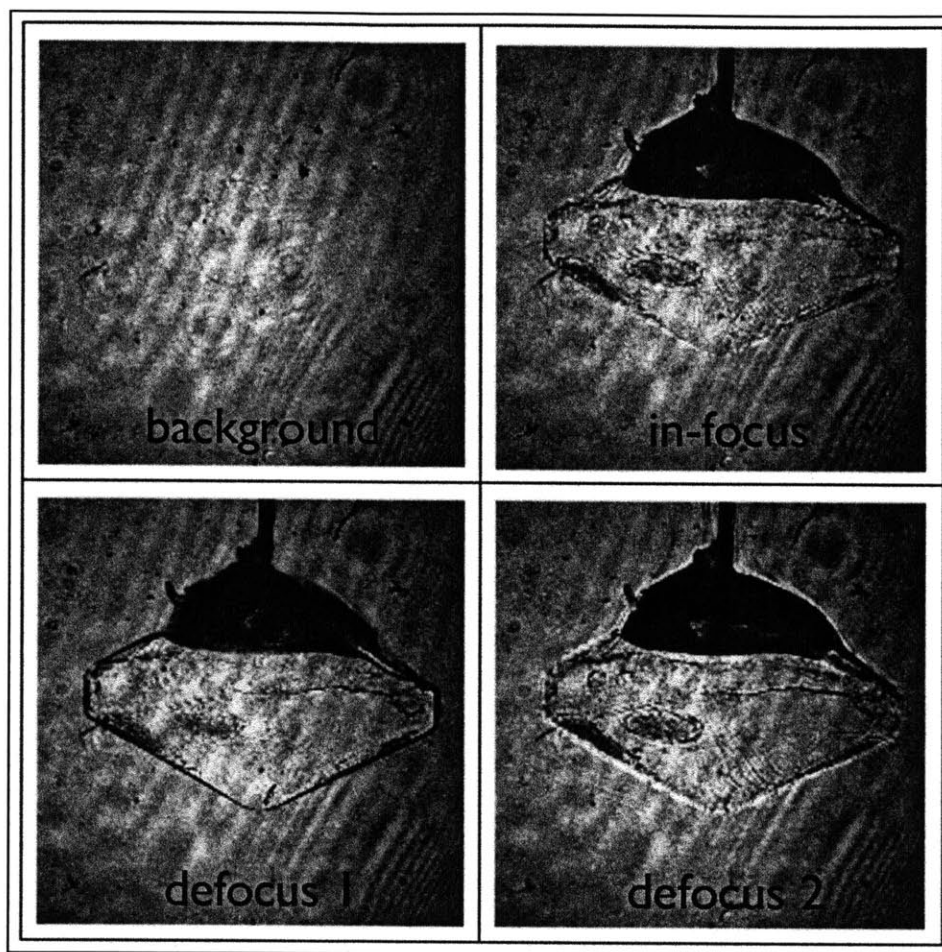


Figure 5-4: Images were captured in-focus, over-focused, and under-focused. Background-subtraction was applied via pixel-wise division before processing.

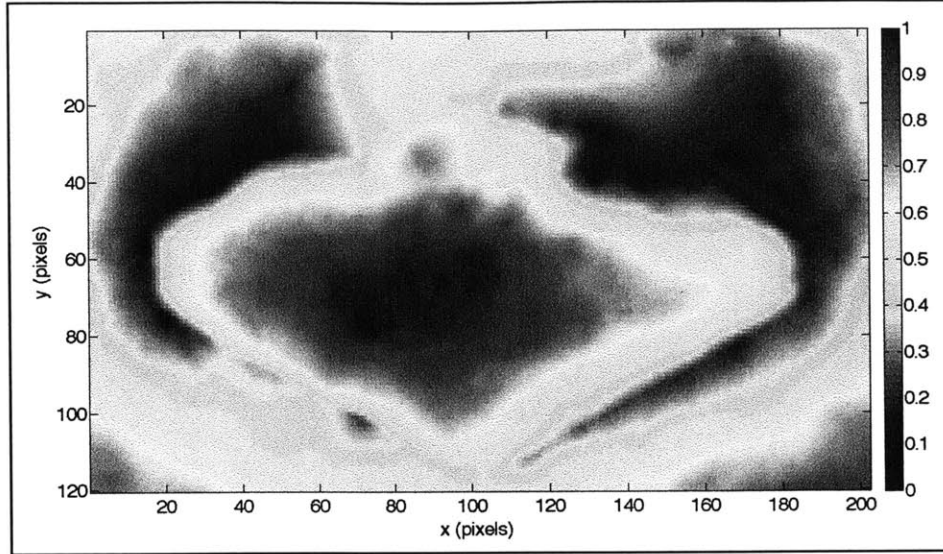


Figure 5-5: Applying the Transport of Intensity Equation to the defocused images results in a phase map representing the approximate phase depth/thickness of the object.

After capture, the images were normalized via pixel-wise division by the background (Figure 5-4). The background-subtracted intensity images were then used to reconstruct three-dimensional refractive index distributions. Tomographic TIE results were retrieved by application of the TIE algorithm to each set of images at each angle, followed by tomographic inversion of the phase information by a filtered backprojection method.

Images and data were processed on a 2.66 Ghz MacBook Pro with 8GB of RAM. The TIE was solved using an FFT-based Fast Poisson Solver, and processing took less than a minute for all view angles. Tomographic reconstruction was performed in a slice-by-slice fashion and took approximately 10 minutes for filtered backprojection (TIE) and 2 hours for backpropagation (IDT). We did not attempt to correct for wobble of the object during rotation (e.g., via image registration) but found the tomographic reconstructions to be relatively insensitive to them.

For the TIE-based method for retrieval of index distribution, phase maps were generated using a simple finite difference method to approximate the derivative of the two intensities with respect to propagation distance. Under the assumption that

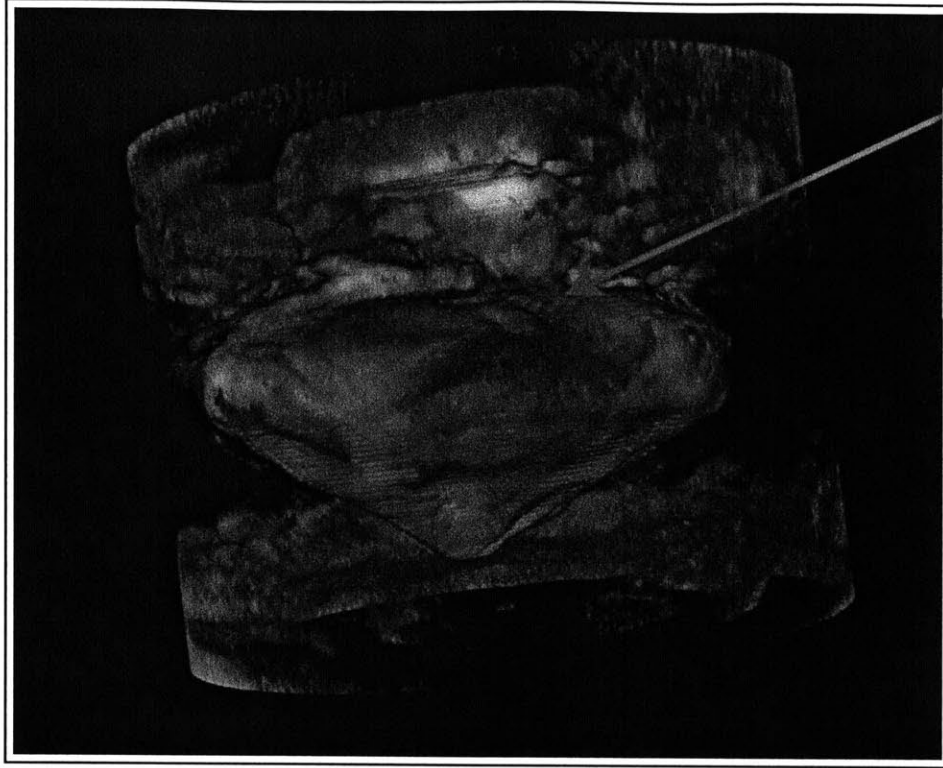


Figure 5-6: Volume-Rendered reconstruction of the object. Features such as edges are discernible.

the object does not scatter and that the intensity at the in-focus plane is constant, the phase maps can be estimated to linearly correlate with the depth of the object ($n \cdot thickness$). For this section of the experiment no attempt was made to account for diffraction.

The 2D Fourier Transforms of these phase maps were placed into Fourier space (sinogram) for slice-by-slice inversion via filtered backprojection. This method is similar to that employed by the authors in [26] to image small optical fibers. The reconstructed object was volumetrically rendered for verification (Figure 5-6). The results show agreement with the general features, shape, and dimensions of the imaged object (diamond). Using a simple threshold/connectivity algorithm for segmentation, the object can be further separated from everything else in the image (Figure 5-7). In contrast, results from tomographic inversion of the raw intensity data (after normalization) are quite poor (Figure 5-8)

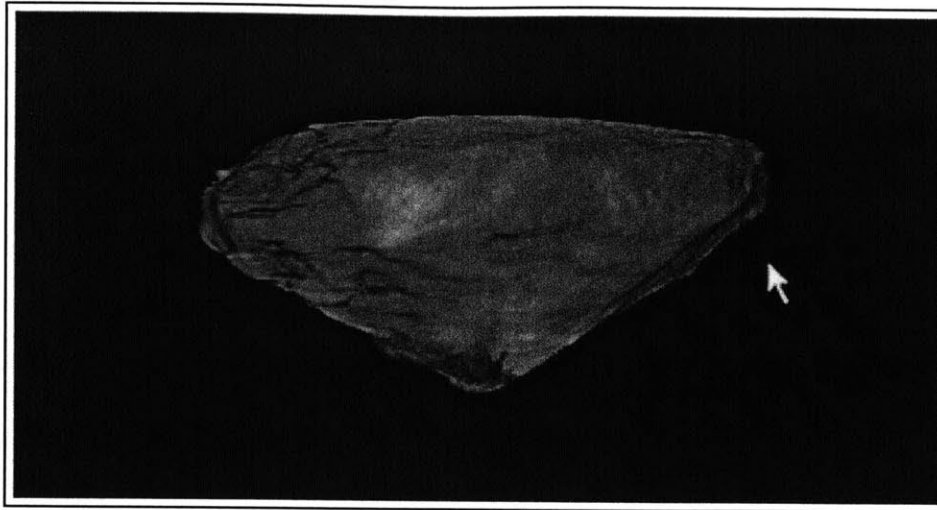


Figure 5-7: Reconstructed Diamond after segmentation via thresholding and connectivity constraints.

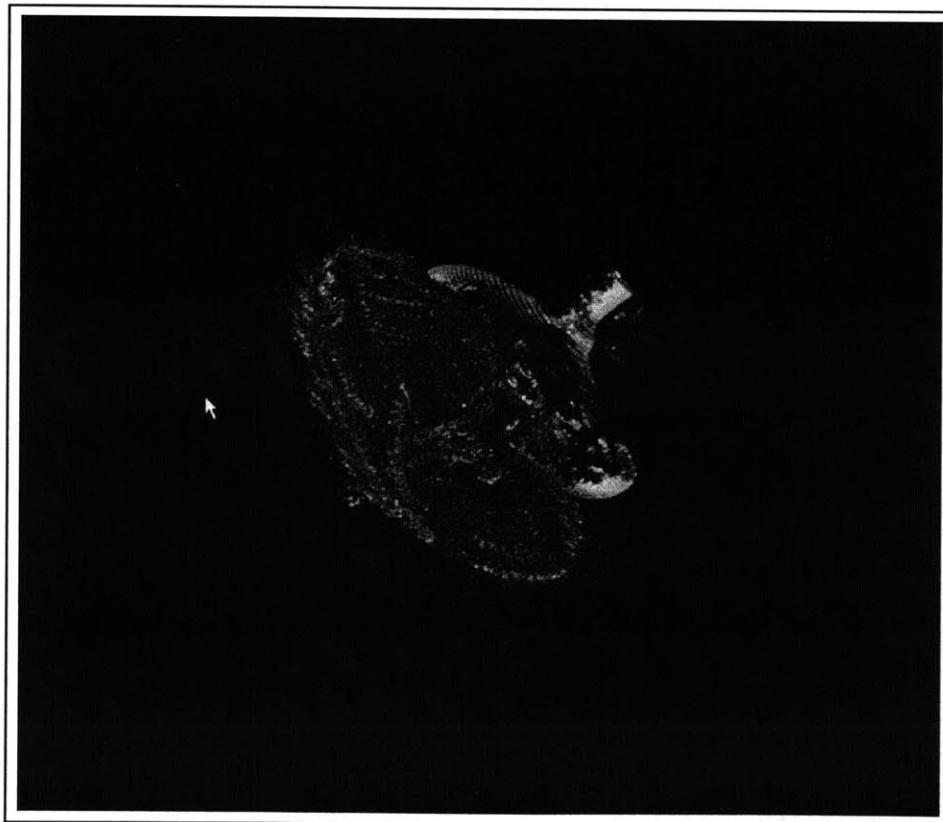


Figure 5-8: Attempts to reconstruct the object from the original images alone result in a “shell” - the edges of a diamond are slightly discernible due to scattering effects, but otherwise the diamond is not detectable

5.3 Measuring the Index of the Diamond

The diamond-shaped object used in this experiment was submerged in an index-matching oil bath of Wessons vegetable oil. The index of refraction of the vegetable oil was measured using an ellipsometer to be $n_{oil} = 1.475 \pm 0.003$ for 632.8nm light. In order to measure the index of refraction of the diamond, a thin layer was sectioned with an Ultracut E ultramicrotome and fixed to a silicon substrate for index measurement via ellipsometry. The diamond section was still thick after slicing to be used in a commercial ellipsometer for thin films, so a custom index measurement system/ellipsometer had to be built to measure the index of refraction of the diamond.

The system setup for index measurement is shown in Figure 5-9. An incident unpolarized laser light source (532 nm) was passed through a linear polarized to independently probe the diamond surface (assumed to be flat) with p-polarized and s-polarized light across a spectrum of angles. Based on the observed reflectance intensities at each angle of incidence (and for each polarization), an estimate for the index of refraction of the diamond was obtained. Specifically, the index was retrieved by optimization of the curve-fit for the Fresnel Equations to the data collected.

The measured/collected data is shown in Table 5.1 (maximum intensity was 0.91 ± 0.03 when no diamond was present in the imaging system), and the curve-fits for the data are shown in Figures 5-10 and 5-11 (s-polarized and p-polarized, respectively). The index of refraction obtained using this method was shown to be $n_{diamond} \approx 1.48 \pm 0.03$. For purposes of this experiment, the diamond was assumed to be homogenous.

5.4 Intensity Diffraction Tomography

Gbur and Wolf previously presented a hybrid intensity-based diffraction tomography model that requires only that the lowest order perturbation of the phase of the field remains paraxial (as opposed to the field being paraxial [48, 49]). Under the first order Rytov approximation, a low-pass filtered estimate of the scattering potential can be retrieved via the following methodology [48, 49, 12]:

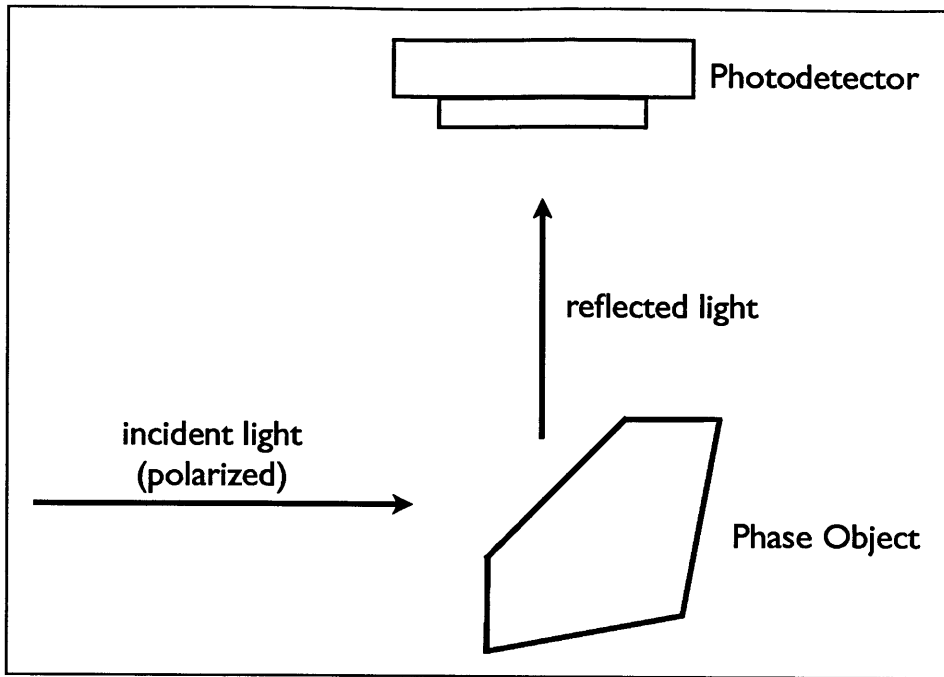


Figure 5-9: Setup: Measurement of Fresnel Reflection Coefficients

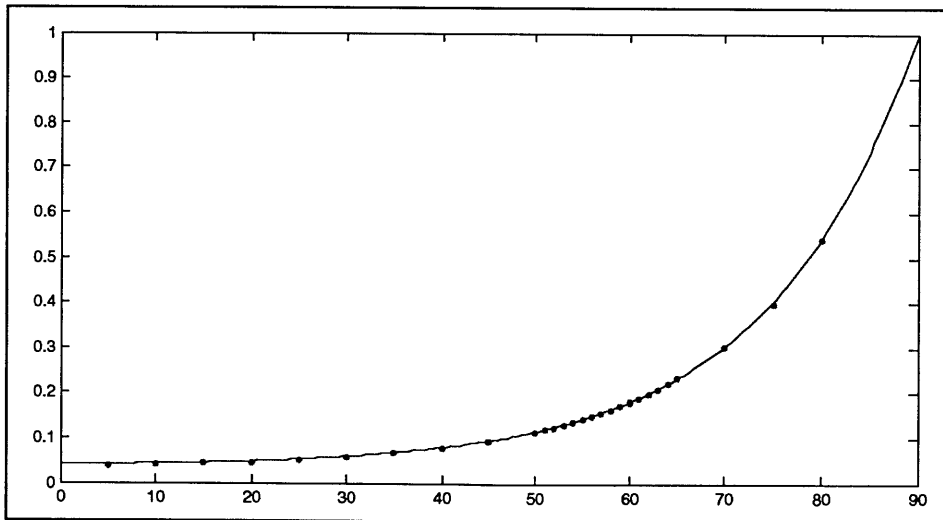


Figure 5-10: Fresnel coefficient curve-Fitting for s-polarized light. x-axis is angle of incidence/reflection, y-axis is normalized intensity ratio

Angle (degrees)	s-polarized (74)	p-polarized (164)
5	0.0354	0.035
10	0.0363	0.0339
15	0.0387	0.032
20	0.0415	0.0296
25	0.0458	0.0268
30	0.0521	0.0227
35	0.06015	0.0182
40	0.0702	0.013
45	0.0847	0.0082
50	0.1037	0.0032
51	0.10855	0.0023
52	0.1128	0.0017
53	0.1179	0.0011
54	0.1231	0.0004
55	0.1285	0
56	0.1349	0
57	0.1413	0
58	0.1484	0
59	0.1554	0.0004
60	0.1636	0.0009
61	0.1720	0.0019
62	0.181	0.0034
63	0.1900	0.0048
64	0.2011	0.0074
65	0.2119	0.0104
70	0.2756	0.0358
75	0.36255	0.09105
80	0.4923	0.2024

Table 5.1: Data collected for index measurement based on Fresnel Coefficient. Incident light had an intensity value of 0.91 ± 0.01

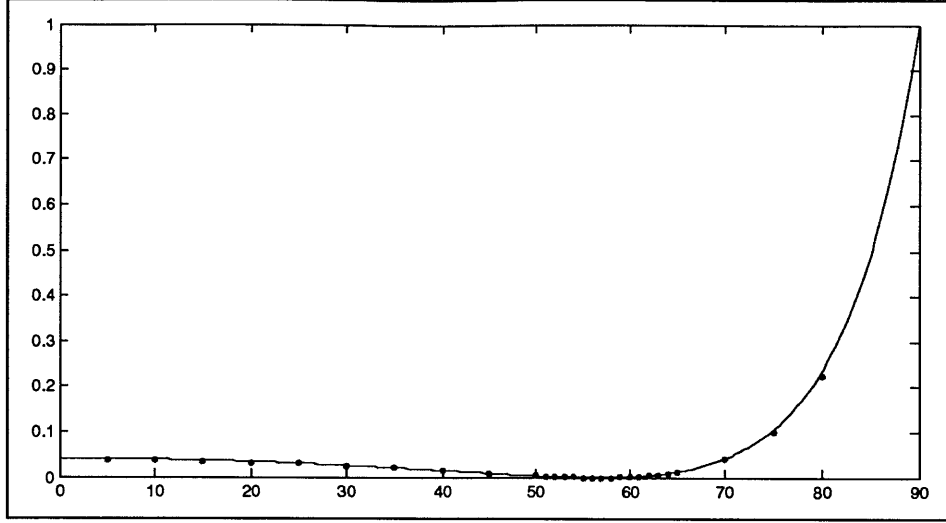


Figure 5-11: Fresnel coefficient curve-fitting for p-polarized light. x-axis is angle of incidence/reflection, y-axis is normalized intensity

In high-frequency applications, only the wavefield intensities, $I(x, y, z) = |U(x, y, z)|^2 = e^{(\Phi + \Phi^*)}$ are measurable. From the intensity, one can define an IDT intensity data function as [48, 49]:

$$d_I(x, y, z) \equiv \log[I(x, y, z)] = \Phi(x, y, z) + \Phi^*(x, y, z) \quad (5.1)$$

Taking two intensity measurements, $I(x, y; z = d)$ and $I(x, y; z = d + \Delta)$, on two detector plants at distances of d and $d + \Delta$, respectively, from the scattering potential at a given tomographic viewing angle, one can define the data functions $d_I(x, y; z = d)$, and $d_I(x, y; z = d + \Delta)$ completely.

In accordance with the derivation in [48], a second data function can be defined as follows [48, 49, 12]:

$$\tilde{D}_\Delta(u, v; d) \equiv \tilde{D}_I(u, v; d) - \tilde{D}_I(u, v; d + \Delta)e^{j(\omega - k)\Delta} \quad (5.2)$$

where \tilde{D}_I represents the 2D Fourier Transform of $d_I(x, y; z)$ for a given plane of constant z . By ignoring evanescent components (i.e., components where $u^2 + v^2 \leq k^2$),

and provided that the planes of intensity measurement are sufficiently close, it can be shown that [48, 49, 12]:

$$\tilde{D}_{\Delta}(u, v; d) \equiv \frac{(2\pi)^2 j}{w} F(u\hat{s}_1 + v\hat{s}_2 + (w - k)\hat{s}_0) e^{j(w-k)d} \{1 - e^{2j(w-k)\Delta}\} \quad (5.3)$$

The above equation has a similar form to that of the Fourier Diffraction Theorem and is known as the IDT Fourier Diffraction Theorem [12]. The IDT Fourier Diffraction Theorem can be used to directly reconstruct a low-pass filtered estimate of scattering potential, $f(\mathbf{r})$, from knowledge of the wavefield intensities on two parallel detector planes at each tomographic view angle. We employ this theorem in conjunction with a back-propagation algorithm introduced in [6] to reconstruct three-dimensional complex index distribution.

For intensity diffraction tomography, the data function from Equation 5-2 was placed into a modified Fourier-space sinogram, and inversion to obtain the complex refractive index of the object was performed using a back-propagation algorithm from [24] and [13]. The index contrast was retrieved and adjusted to give absolute index based on ellipsometry measurements of the index of the surrounding media ($n_{media} = 1.475$).

5.5 Measuring Diamond Dimensions

The dimensions of the diamond were measured with a digital caliper. The object was assumed to be circularly symmetric, and the caliper measurements were confirmed to be in agreement with the observable object outline from in-focus images taken of the diamond. Caliper measurements of the diamond were 5.9mm for object height and 12.0mm for object width. Figure 5-12 shows a rough schematic of the diamond

5.6 Comparison of Reconstructions

The figures in this section compare the quality of reconstructions from (1) direct tomographic inversion without phase retrieval, (2) TIE-based tomography, and (3)

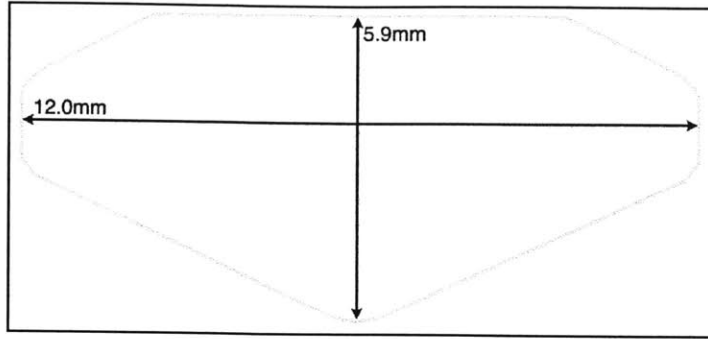


Figure 5-12: Diamond Schematic. The shape of the diamond was approximated from the object outline in the in-focus image, and object dimensions were measured with a caliper.

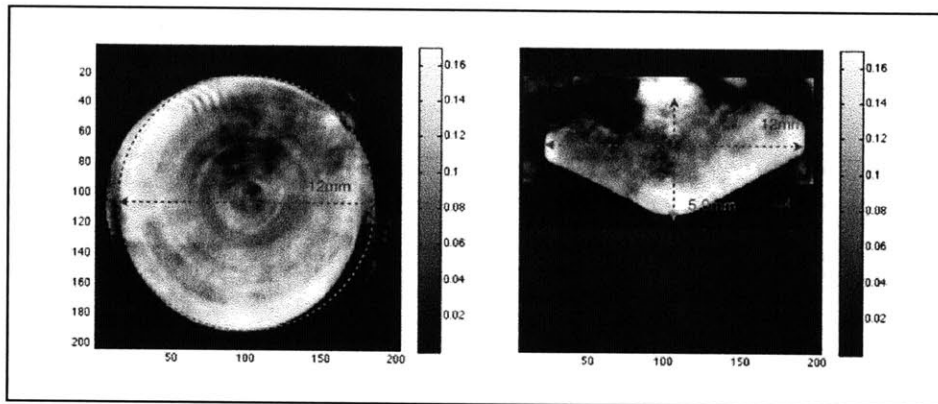


Figure 5-13: The TIE-based reconstruction does not match the dimensions of the diamond very well.

Intensity-Based Diffraction Tomography.

In theory, if the field is paraxial enough, then the TIE and IDT cases should be equivalent (If the transmitted field is paraxial, then reconstruction using IDT is equivalent to placing the TIE-retrieved field into arcs in Fourier Space and applying the Fourier Diffraction Projection Theorem). Anastasio proves this in [12], and a recapitulation of his proof is in the appendix.

5.7 Compressive Intensity Tomography

Compressive sensing was simulated on different setups of diffraction tomography to estimate what the quality of reconstructions might look like. The results for compres-

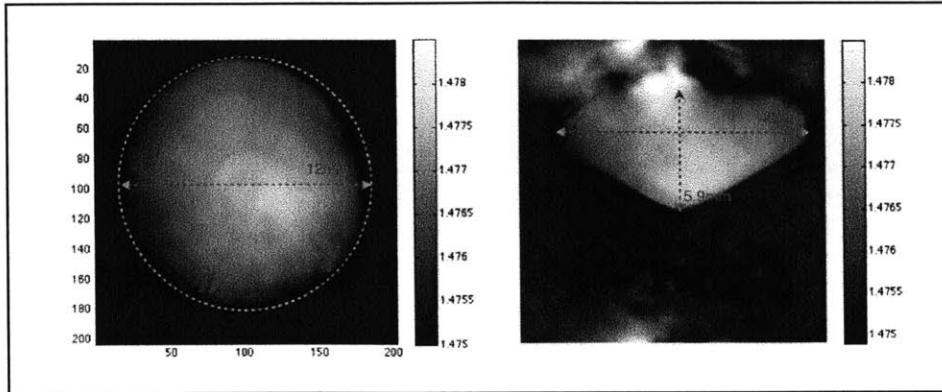


Figure 5-14: The IDT-based reconstruction more accurately matches the dimensions of the diamond.

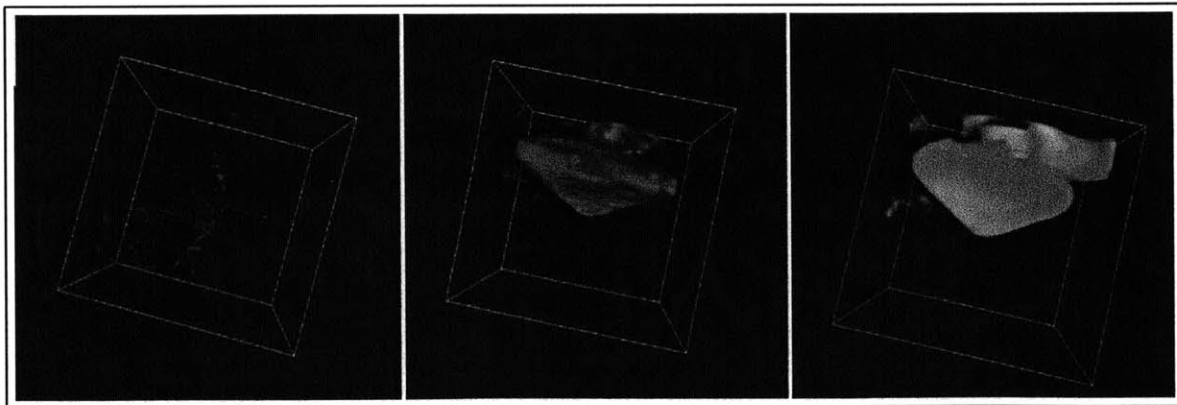


Figure 5-15: Volumetric reconstruction of object: (left) without TIE or IDT (middle) with TIE (right) with IDT. The TIE reconstruction has more well-defined edges, but the volume/dimensions of the object reconstructed is not as accurate as that in the IDT reconstruction

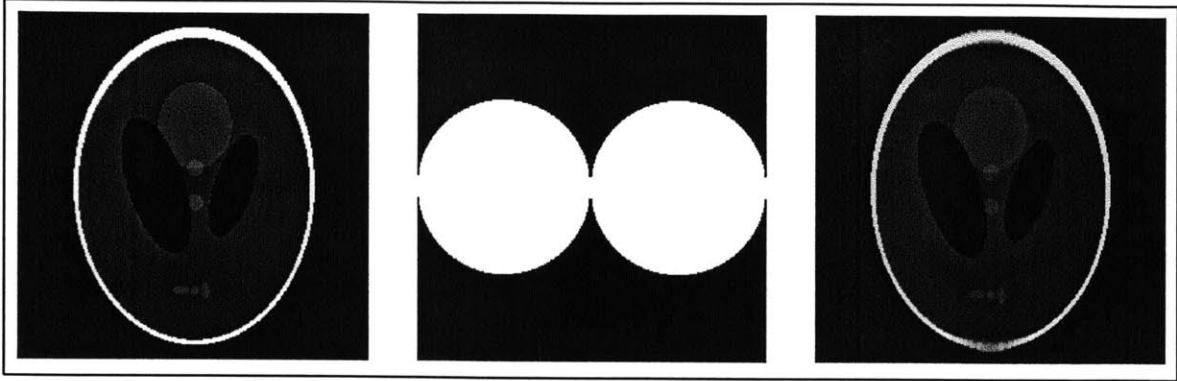


Figure 5-16: Compressive Diffraction Tomography reconstruction from limited view-angles. (left) original image. (middle) Fourier-space coverage from synthetic aperture diffraction tomography, (right) recovered image

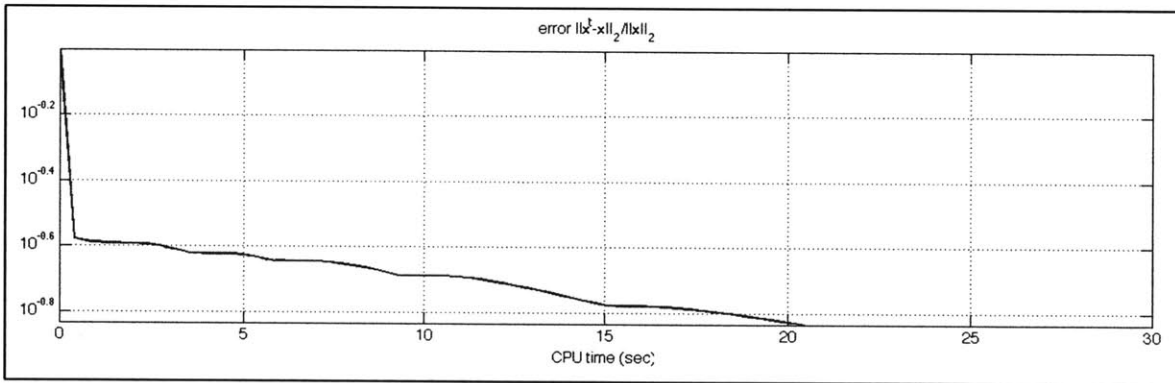


Figure 5-17: Convergence of the Compressive Sensing Solver, TwIST

sive tomography and compressive diffraction tomography are shown in Figure 4-5 in Chapter 4. The results from limited-angle tomography (as in the scanning/synthetic aperture system detailed in chapter 2) are shown below for the ideal case. A plot of the reconstruction accuracy convergence rate is shown below as well. While requiring gridding to work, the method used for the simulated data returns results that are significantly better than those obtained via the methodology of [69] and [70]

5.8 Conclusions and Extensions: Toward Real-Time Phase Tomography

This work demonstrates 3-Dimensional tomography of a phase object using transport of intensity principles. In this work, intensity changes/variations within a volume where measured by manually moving the detector (e.g., via placing it on a linear stage). If this movement could be avoided (and multi-plane measurements made simultaneously), then one could design a system capable of real-time phase retrieval. Coupling real-time phase retrieval with rapid 360-degree rotation about the object would yield a system capable of real-time phase tomography.

5.8.1 Dual-camera TIE

Perhaps the simplest method for acquiring images at multiple planes simultaneously would be to simply split the post-object wavefront and use two cameras as detectors in the system (placed at different distances from the object). In practice, it is extremely difficult to align the images from the two camera using traditional image registration techniques (minimizing L2 difference, minimizing/maximizing cross-correlation, minimizing joint entropy/maximizing mutual information, etc.).

5.8.2 SLM-based defocus system

To avoid these issues of alignment, one could use a spatial light modulator (SLM) to computationally defocus the light (thereby capturing multiple planes of intensity in “real-time”). This could be technically challenging to do since the SLM must be properly calibrated and have fine enough pixel resolution to defocus (Note: SLM-based defocusing can be performed in the Fourier domain as well with the proper placement of lenses.)

Waller et al. have explored two other novel methods for acquiring multi-plane images for real-time transport-of-intensity-based phase retrieval. They are discussed

briefly below:

5.8.3 Volume Holographic TIE Tomography

This system capitalizes on the ability of a volume holographic imaging system to image multiple planes at the same time. A thick (“volume”) hologram is placed at the pupil plane of a 4f system, and the Bragg selectivity of the volume hologram is utilized to image a single depth of an object (angular selectivity at the Fourier plane). If the volume hologram is multiplexed, than multiple planes can be imaged at the same time. Waller et al. in [74] use this setup to acquire images at multiple depths to retrieve the phase depth of a phase object. This method suffers the same problems that dual-camera TIE faces with image registration.

5.8.4 Color TIE Tomography

This setup utilizes chromatic aberrations in lenses and reformulates the TIE to a color-modified version. From a single color-image, the red, green, and blue channels will be either: over-focused, in-focus, or under-focused to a degree depending on the amount of chromatic aberration present in the system. Based on the over and under-focused data, one can retrieve phase using a modified TIE derived in [72]. The authors in [73] have demonstrated this system’s use for real-time phase retrieval.

5.8.5 Application Real-time phase imaging flow cytometer

One potentially significant application of real-time phase-retrieval from intensity measurements would be in a flow cytometry setup. One could imagine a phase-imaging system that rotates around a “ring” (similarly to modern CT scanners) to capture “slices” of the object of interest in real-time. Since the cells are flowing at some fixed rate in flow cytometers, their movement by this ring would allow for acquisition of 3-dimensional phase data. Such a system could significantly improve our understanding of live cells and pathology.

Appendix A

Derivations

A.1 TIE Derivation

Paraxial TIE derivation (Teague 1983).

$$(j \frac{\partial}{\partial z} + \frac{\nabla^2}{2k} + k)u_z(\mathbf{r}) = 0 \quad (\text{A.1})$$

$$j(u^* \frac{\partial u}{\partial z} + u \frac{\partial u^*}{\partial z}) + \frac{1}{2k}(\nabla(u^* \nabla u - u \nabla u^*)) = 0 \quad (\text{A.2})$$

$$u = \sqrt{I(z)}e^{j\phi(z)} = E_0(z)e^{j\phi(z)} \quad (\text{A.3})$$

$$u^* = E_0^*(z)e^{-j\phi(z)} \quad (\text{A.4})$$

$$\nabla u = (u)(j\nabla\phi) \quad (\text{A.5})$$

$$\nabla u^* = (u^*)(-j\nabla\phi) \quad (\text{A.6})$$

$$u^* \nabla u = (u^*)(u)(j\nabla\phi) = jI(z)\nabla\phi \quad (\text{A.7})$$

$$u \nabla u^* = (u)(u^*)(-j\nabla\phi) = -jI(z)\nabla\phi \quad (\text{A.8})$$

$$(u^* \nabla u - u \nabla u^*) = 2jI(z)\nabla\phi \quad (\text{A.9})$$

$$j(u^* \frac{\partial u}{\partial z} + u \frac{\partial u^*}{\partial z}) = j(\frac{\partial}{\partial z}(uu^*)) = j \frac{\partial I}{\partial z} \quad (\text{A.10})$$

$$k \frac{\partial I}{\partial z} = -\nabla(I\nabla\phi) \quad (\text{A.11})$$

A.2 TIE-IDT equivalence [12]

IDT-equivalent TIE equation: $\nabla_{\perp}^2 \Phi_i(x, y, z) = -\frac{k}{I(x, y, z)} \frac{\partial}{\partial z} I(x, y, z)$

TIE equation: $-k \frac{\partial I(x, y, z)}{\partial z} = \nabla_{\perp} \cdot (I(x, y, z) (\nabla_{\perp} \cdot \Phi_i(x, y, z)))$

The proof of IDT-TIE equivalence in the paraxial regime is given in [12] and shown below:

If the transmitted wavefield ($U(x, y, z) = U_i(z, y, z)e^{\Phi}$) is paraxial, then $|\Phi(x, y, z)| \ll 1$.

1. The TIE posits that:

$$-k \frac{\partial}{\partial z} I(x, y, z) = \nabla_{\perp} I(x, y, z) \cdot \nabla_{\perp} \Phi_i(x, y, z) + I(x, y, z) \nabla_{\perp}^2 \Phi_i(x, y, z). \quad (\text{A.12})$$

where $\nabla_{\perp} \equiv \frac{\partial}{\partial x} \hat{s}_1 + \frac{\partial}{\partial y} \hat{s}_2$. Under Rytov approximation, the above equation can be re-expressed as:

$$-k \frac{1}{I(x, y, z)} \frac{\partial}{\partial z} I(x, y, z) = \nabla_{\perp} \log I(x, y, z) \cdot \nabla_{\perp} \Phi_i(x, y, z) + \nabla_{\perp}^2 \Phi_i(x, y, z) \quad (\text{A.13})$$

or equivalently,

$$-k \frac{1}{I(x, y, z)} \frac{\partial}{\partial z} I(x, y, z) = 2 \nabla_{\perp} \Phi_r(x, y, z) \cdot \nabla_{\perp} \Phi_i(x, y, z) + \nabla_{\perp}^2 \Phi_i(x, y, z). \quad (\text{A.14})$$

IDT reconstruction theory assumes the validity of the first-order Rytov approximation for wave propagation in an inhomogeneous medium and thus requires that $\nabla \Phi(x, y, z) \cdot \nabla \Phi(x, y, z) \approx 0$ in the entire medium (throughout the scattering potential and surrounding media). This statement implies that:

$$\nabla \Phi_r(x, y, z) \cdot \nabla \Phi_r(x, y, z) + \nabla \Phi_i(x, y, z) \cdot \nabla \Phi_i(x, y, z) \approx 0 \quad (\text{A.15})$$

and also that:

$$\nabla_{\perp} \Phi_r(x, y, z) \cdot \nabla_{\perp} \Phi_r(x, y, z) + \nabla_{\perp} \Phi_i(x, y, z) \cdot \nabla_{\perp} \Phi_i(x, y, z) \approx 0 \quad (\text{A.16})$$

everywhere. By use of the inequality:

$$|2\nabla_{\perp}\Phi_r(x, y, z)\cdot\nabla_{\perp}\Phi_i(x, y, z)| \leq \nabla_{\perp}\Phi_r(x, y, z)\cdot\nabla_{\perp}\Phi_r(x, y, z)+\nabla_{\perp}\Phi_i(x, y, z)\cdot\nabla_{\perp}\Phi_i(x, y, z) \quad (\text{A.17})$$

one finds that the term $2\nabla_{\perp}\Phi_r(x, y, z)\cdot\nabla_{\perp}\Phi_i(x, y, z)$ to be negligible in equation X. Thus, if the wavefield is paraxial and the first-order Rytov approximation is valid (everywhere), then the TIE and IDT equations are equivalent.

Bibliography

- [1] C.J.R. Sheppard, and T. Wilson, "Fourier Imaging of Phase Information in Scanning and Conventional Optical Microscopes" *Royal Society of London Philosophical Transactions Series A*, vol. 295, pp 513-536, 1980
- [2] C.J.R. Sheppard, "Defocused transfer function for a partially coherent microscope" *Journal of the Optical Society of America*, vol. 21, no. 5, 2004
- [3] D. W. Sweeney and C. M. Vest, "Reconstruction of Three-Dimensional Refractive Index Fields from Multidirectional Interferometric Data," *Applied Optics*, Vol. 12, No. 11, 1973.
- [4] Jerrold T. Bushberg, J. Anthony Seibert, Edwin M. Leidholdt Jr., and John M. Boone, *Essential Physics of Medical Imaging*, Lippincott Williams & Wilkins, 2001.
- [5] M. Born and E. Wolf, *Principles of Optics: Electromagnetic Theory of Propagation, Interference and Diffraction of Light*. Cambridge University Press, 7th ed., 1999
- [6] A.C. Kak and M. Slaney, *Principles of Computerized Tomographic Imaging*. IEEE Press, 1994.
- [7] K. A. Nugent, T. E. Gureyev, D. F. Cookson, D. Paganin, and Z. Barnea, "Quantitative Phase Imaging Using Hard X Rays," *Phys. Rev. Lett.*, 0031-9007/96/77(14)/2961(4), 1996.

- [8] M.R. Teague, “Deterministic phase retrieval: a Green’s function solution”, *J. Opt. Soc. Am.*, 73, 1434-1441, 1983.
- [9] Keith A. Nugent, David Paganin, and Tim E. Gureyev, “A Phase Odyssey,” *Physics Today*, August, 2001.
- [10] G. Gbur, E. Wolf, “Hybrid diffraction tomography without phase information”. *J. Opt. Soc. Am. A*, 19, 2194-2202, 2002.
- [11] G. Gbur, E. Wolf, “Diffraction tomography without phase information” *Opt. Lett.*, 27, 1890-1892, 2002.
- [12] M.A. Anastasio and D. Shi, “On the Relationship between Intensity Diffraction Tomography and Phase-Contrast Tomography”, *Proc. SPIE*. 5535, 361-367, 2004.
- [13] Xiaochuan Pan “Unified reconstruction theory for diffraction tomography, with consideration of noise control” *J. Opt. Soc. Am. A*, Vol. 15, No. 9 1998.
- [14] John Pauly, “Non-Cartesian Reconstruction” *Course Notes*, 2007.
- [15] Wonshik Choi, Christopher Fang-Yen, Kamran Badizadegan, Ramachandra R. Dasari, and Michael S. Feld, “Extended depth of focus in tomographic phase microscopy using a propagation algorithm,” *Optics Letters*, Vol. 33, No. 2, 2008.
- [16] Wonshik Choi, Christopher Fang-Yen, Kamran Badizadegan, Seungeun Oh, Niyom Lue, Ramachandra R Dasari, and Michael S Feld, “Tomographic phase microscopy,” *Nature Methods*, August, 2007.
- [17] Yongjin Sung, Wonshik Choi, Christopher Fang-Yen, Kamran Badizadegan, Ramachandra R. Dasari, and Michael S. Feld, “Optical diffraction tomography for high resolution live cell imaging,” *Optics Express*, Vol. 17, No. 1, 2009.
- [18] Torolf C. Wedberg and Jakob J. Stamne , “Experimental examination of the quantitative imaging properties of optical diffraction tomography,” *J. Opt. Soc. Am.*, Vol. 12, Issue 3, 1995.

- [19] D. Ghiglia and M. Pritt, *Two-dimensional phase unwrapping: theory, algorithms and software*. Wiley Blackwell, 1998
- [20] D. Ghiglia and L. Romero, “Robust two-dimensional weighted and unweighted phase unwrapping that uses fast transforms and iterative methods” *Journal of the Optical Society of America*, Vol. 11, No. 1, 1994
- [21] Joseph W. Goodman, *Introduction to Fourier Optics*, Roberts & Company Publishers, 2004
- [22] R. P. Porter and A. J. Devaney, “Holography and the inverse source problem,” *J. Opt. Soc. Am.*, 72, 327, 1982.
- [23] D. Paganin and K. Nugent, “Noninterferometric phase imaging with partially coherent light,” *Phys. Rev. Lett.*, 80, 25862589, 1998.
- [24] M.A. Anastasio, “Computationally efficient and statistically robust image reconstruction in three-dimensional diffraction tomography” *J. Opt. Soc. Am.*. A 17, 391-400, 2000.
- [25] N. Streibl, “Phase imaging by the transport equation of intensity”, *Opt. Commun.*, 49, 610, 1984.
- [26] A. Barty, K.A. Nugent, A.R. Roberts, and D. Paganin., “Quantitative phase tomography”, *Optics Communications*, 175, 329-336, 2000.
- [27] E. Barone-Nugent, A. Barty, and K. Nugent, “Quantitative phase-amplitude microscopy I: optical microscopy” *J. Microsc.*, 206, 194203, 2002.
- [28] D. Paganin, A. Barty, P. J. McMahon, and K. A. Nugent, “Quantitative phase-amplitude microscopy. III. The effects of noise”, *J. Microsc.*, 214, 5161, 2004.
- [29] T. Gureyev and K. Nugent, “Rapid quantitative phase imaging using the transport of intensity equation” *Opt. Commun.*, 133, 339346, 1997.
- [30] L. Allen and M. Oxley, “Phase retrieval from series of images obtained by defocus variation” *Opt. Commun.*, 199, 6575, 2001.

- [31] E. Candes, J. Romberg, and T. Tao, “Stable signal recovery from incomplete and inaccurate measurements,” *Comm. Pure Appl. Math*, 2006.
- [32] D. L. Donoho, “Compressed sensing,” *IEEE Transactions on Information Theory*, 52(4), 1289-1306 2006.
- [33] D. L. Donoho, “Communications in the presence of noise,” *Proc.of the IRE*, 5v 37, 1021 1949.
- [34] E. J. Cands, M. Rudelson, T. Tao and R. Vershynin, “Error correction via linear programming,” *Proceedings of the 46th Annual IEEE Symposium on Foundations of Computer Science (FOCS)*, 295-308 2005.
- [35] E. J. Candes and J. Romberg, “Sparsity and incoherence in compressive sampling,” *Inverse Problems*, 23 969-985 2006.
- [36] E. J. Candes and J. Romberg, “The restricted isometry property and its implications for compressed sensing.,” *Compte Rendus de l’Academie des Sciences, Paris, Serie I*, 346 589-592 2008.
- [37] D. Takhar et al., “A new compressive imaging camera architecture using optical-domain compression.,” *Computational Imaging IV*, 2006
- [38] E. J. Candes and Y. Plan., “Matrix completion with noise.,” *Proceedings of the IEEE*, 2009
- [39] S. Becker, J. Bobin, and E. J. Candes, “NESTA: a fast and accurate first-order method for sparse recovery,” *SIAM J. on Imaging Sciences*, 2009
- [40] J.M.Bioucas-Dias and M.A.T.Figueiredo, “A new twist: Two step iterative shrinkage/thresholding algorithms for image restoration,” *IEEE Transactions on Image Processing*, 16, 2992-3004, 2007
- [41] H. Sun et al., “Underwater digital holography for studies of marine plankton,” *Phil. Trans. R. Soc. A*, vol. 366 no. 1871, 2008

- [42] S. Coetmellec et al., “Application of in-line digital holography to multiple plane velocimetry,” *Meas. Sci. Technol.*, 12 1392, 2001
- [43] W. Xu et al., “Digital in-line holography for biological applications,” *Proc. Nat. Acad. Sci.*, vol. 98 no. 20, 2001
- [44] U. Schnars and W. Jueptner, *Digital holography*. New York: Springer, 2004
- [45] C. Barsi, W. Wan, and J. W. Fleischer, “Imaging through nonlinear media using digital holography,” *Nature Photonics*, vol. 3, pp. 211-215, 2009
- [46] C. McElhinney et al., “Twin-image reduction in inline digital holography using an object segmentation heuristic,” *J. Phys.: Conf. Ser.*, 2008
- [47] T. Latychevskaia and H. W. Fink, “Solution to the Twin Image Problem in Holography,” *Phys. Rev. Lett.*, 2007
- [48] G. Gbur, E. Wolf, “Hybrid diffraction tomography without phase information,” *J. Opt. Soc. Am. A.*, 2002
- [49] G. Gbur, E. Wolf, “Diffraction tomography without phase information,” *Opt. Lett.*, 2002
- [50] Laura Waller, Lei Tian, and George Barbastathis, “Transport of Intensity Imaging with Higher Order Derivatives”, *Computational Optical Sensing and Imaging, OSA Technical Digest*, paper CThA3, 2009.
- [51] T.E. Gureyev, A. Roberts, and K.A. Nugent, “Partially coherent fields, the transport of intensity equation, and phase uniqueness”, *J. Opt. Soc. Am. A*, 12, 1942-1946, 1995.
- [52] R. P. Porter and A. J. Devaney, “Holography and the inverse source problem,” *J. Opt. Soc. Am.*, 72, 327, 1982.
- [53] M. Slaney, A.C. Kak, and L.E. Larsen, “Limitations of imaging with first-order diffraction tomography,” *IEEE Transactions on Microwave Theory Techniques*, 32, 860874, 1984.

- [54] W. Li, N. Loomis, Q. Hu, and C. S. Davis, “Focus detection from digital in-line holograms based on spectral L1 norms,” *J. Opt. Soc. Am. A*, 24, 30543062, 2007.
- [55] L. Tian, N. Loomis, J. A. Domnguez-Caballero, and G. Barbastathis, “Quantitative measurement of size and three-dimensional position of fast-moving bubbles in air-water mixture flows using digital holography,” *Appl. Opt.*, 49, 15491554, 2010.
- [56] D. J. Brady, K. Choi, D. L. Marks, R. Horisaki, and S. Lim, “Compressive holography,” *Opt. Express*, 17, 13,04013,049 2009.
- [57] L. Denis, D. Lorenz, E. Thiébaud, C. Fournier, and D. Trede, “Inline hologram reconstruction with sparsity constraints,” *Opt. Lett.*, 34, 34753477, 2009.
- [58] J. Katz and J. Sheng, “Applications of holography in fluid mechanics and particle dynamics,” *Annual Review of Fluid Mechanics*, 42, 531555, 2010.
- [59] J. M. Bioucas-Dias and M. A. T. Figueiredo, “New TwIST: Two-Step Iterative Shrinkage/Thresholding algorithms for image restoration,” *IEEE Transactions on Image Processing*, 16, 29923004, 2007.
- [60] M. Beleggia, M. A. Schofield, V. V. Volkov, Y. Zhu, “On the transport of intensity technique for phase retrieval,” *Ultramicroscopy*, 102, 3749, 2004.
- [61] Mark A. Anastasio, Daxin Shi, Yin Huang, and Greg Gbur. “Image reconstruction in spherical-wave intensity diffraction tomography” *J. Opt. Soc. Am. A*, Vol. 22, No. 12, 2005.
- [62] Jing Cheng and Shensheng Han. “Diffraction tomography reconstruction algorithms for quantitative imaging of phase objects,” *J. Opt. Soc. Am. A*, Vol. 18, No. 7 2001.
- [63] Mark A. Anastasio, Qiaofeng Xu, and Daxin Shi. “Multispectral intensity diffraction tomography: single material objects with variable densities,” *J. Opt. Soc. Am. A*, Vol. 26, No. 2, 2009.

- [64] Yin Huang and Mark A. Anastasio. "Image reconstruction in lens-based intensity diffraction tomography," *J. Opt. Soc. Am. A*, Vol. 26, No. 6 2009.
- [65] Torolf C Wedberg and Jakob J Stamnes, "Comparison of phase retrieval methods for optical diffraction tomography" *Pure Appl. Opt.*, 4, 39-54, 1995.
- [66] Brent L. Bachim and Thomas K. Gaylord, "Microinterferometric optical phase tomography for measuring small, asymmetric refractive-index differences in the profiles of optical fibers and fiber devices," *Appl. Opt.*, Vol. 44, No. 3 2005.
- [67] Florian Charrire, Nicolas Pavillon, Tristan Colomb, Christian Depeursinge, Thierry J. Hegera, Edward A.D. Mitchel, Pierre Marquet, and Benjamin Rappaz. "Living specimen tomography by digital holographic microscopy: morphometry of testate amoeba" *Optics Express*, Vol. 14, No. 16, 2006.
- [68] Laura Waller and George Barbastathis, "Error Analysis of Phase-Shifting for Phase and Amplitude Tomographic Reconstruction," *Computational Optical Sensing and Imaging, OSA Technical Digest. CTuB5*, 2007.
- [69] Samuel J. LaRoque, Emil Y. Sidky, and Xiaochuan Pan, "Accurate image reconstruction from few-view and limited-angle data in diffraction tomography" *J. Opt. Soc. Am. A*, Vol. 25, Issue 7, 2008
- [70] Emil Y Sidky, Chien-Min Kao, Xiaochuan Pan, "Accurate image reconstruction from few-views and limited-angle data in divergent-beam CT" *Radiology*, Vol. 14, Issue 2, 2009
- [71] Shan Shan Kou, Laura Waller, George Barbastathis, and Colin J. R. Sheppard, "Transport-of-intensity approach to differential interference contrast (TI-DIC) microscopy for quantitative phase imaging," *Optics Letters*, Vol. 35, No. 3, 2010.
- [72] L. Waller, S.S. Kou, C. Sheppard, G. Barbastathis, "Phase from chromatic aberrations," *Opt. Express*, 18(22) 22817-22825, 2010

- [73] N. Loomis, L. Waller , G. Barbastathis, “High-speed phase recovery using chromatic transport of intensity computation in graphics processing units,” *Proc. OSA Digital Holography conference*, 2010
- [74] L. Waller, Y.Luo, S. Yang, G. Barbastathis, “Transport of Intensity phase imaging in a Volume Holographic Microscope,” *Opt. Lett.*, 35(17) 2961-2963, 2010
- [75] L. Waller, M. Tsang, S. Ponda, G. Barbastathis, “Complex-field estimation by Kalman filtering,” *Opt. Express*, 19(3), 2805-2815, 2011